RELATION BETWEEN SOLITARY WAVE OCCURRENCE AND SOLAR WIND PARAMETERS DURING THE KELVIN-HELMHOLTZ INSTABILITY

By

TYLER L. WORKMAN

THESIS

Submitted in partial fulfillment of the requirements for the degree of Master of Science in Physics at The University of Texas at Arlington
August 2023

Arlington, Texas

Supervising Committee:

Frederick D. Wilder, Supervising Professor

Ramon Lopez

Yue Deng

ABSTRACT

Relation Between Solitary Wave Occurrence and Solar Wind Parameters During the Kelvin-Helmholtz Instability

Tyler L. Workman, M. Phys

The University of Texas at Arlington, 2023

Supervising Professor: Frederick D. Wilder

The Kelvin-Helmholtz instability (KHI) is an important mechanism whereby the solar wind transports energy and momentum into the magnetosphere. One unresolved topic is the role of kinetic phenomena and turbulence in mediating this energy transport. Previous studies hypothesized that the prevalence of electrostatic solitary waves, an artifact of kinetic turbulence, decreased along the flanks as the instability grew. These previous studies had been conducted using 3 KHI events. For this study, we test the hypothesis and further investigate how these solitary waves affect the local plasma with an expanded list of 15 KHI events. A combination of solar wind data from OMNI and in-situ plasma measurements from the NASA Magnetospheric Multiscale (MMS) mission was taken for the duration of these events. Analysis of the findings show that solitary wave occurrence seems to coincide with ion temperature isotropy and electron temperature anisotropy biased to the direction parallel to the magnetic field. It was further observed that solitary wave occurrence was highly negatively correlated with the position of the

KHI event along the magnetospheric flank, supporting the previous hypothesis. Additional correlations to solar wind velocity and pressure were also found.

ACKNOWLEDGEMENTS

I thank my Supervising Committee for their instrumental role in bringing this academic work to fruition. I further would like to thank my Supervising Professor, Dr. Wilder specifically, for his continued patience, guidance, and feedback throughout this study. This work was made possible by the many brilliant minds involved in the Magnetospheric Multiscale mission, the Python adaptation of the SPEDAS program, and the OMNI Database curated by King and Papitashvili for NASA and the Goddard Space Flight Center

DEDICATION

I dedicate this thesis to my Supervising Professor Dr. Wilder, whose work this study expanded upon and whose guidance was vital to bringing this thesis to fruition. I further dedicate this thesis to my mother and father, who raised and encouraged me to pursue my academic interests and who continue to support me. Finally, I dedicate this thesis to my fiancé, without whom I could never have reached where I am today.

LIST OF FIGURES

Figure Page

1. INTRODUCTION

2. METHODOLOGY

3. RESULTS AND DISCUSSION

TABLE OF CONTENTS

CHAPTER

INTRODUCTION

Earth's magnetosphere plays a crucial role in our planet's interactions with the sun, driving many different structures in the upper atmosphere. Notably, the sun contributes a substantial portion of the incoming flow of radiation and plasma, called the "solar wind." The solar wind is the result of the corona being a population of hot plasma in a relative vacuum, allowing for the plasma to escape the confines of the sun's immediate gravity, often at high speeds (*Hundhausen*, 1995).

The study of interactions between the Earth's upper atmosphere and the plasma from the solar wind and magnetosphere is known as "Space Physics." Unlike distant astrophysical bodies, the relative proximity of Earth's magnetosphere allows for in-situ satellite observations, providing the field of space physics with a host of detailed information about plasma phenomena. Understanding the interactions between Earth and its neighbors allows for a deeper understanding of the dynamics of planetary magnetic fields.

1.1 The Solar Wind

The notion of the sun radiating away fast particles was first proposed by *Störmer* (1912), though it was *Chapman and Ferraro* (1931) which truly began to expand that idea into the realm of Earth's Magnetosphere. The developments explored in these areas led *Parker* (1965) to conceptualize and calculate the solar wind interactions as an "expanding atmosphere", while commenting on how the properties of this would interplay with Earth. This choice of conceptualization allows many of the solar wind interactions to be described using fluid theory. More specifically, the solar wind can be described as a Magnetohydrodynamic (MHD) fluid, allowing us to use the relevant formulae. Isolating a portion of the current density formula from Ohm’s law, then using Maxwell’s equations can produce the MHD Induction equation:

$$\frac{\partial B}{\partial t} = \nabla \times (u \times B) - \nabla \times \left(\frac{J}{\sigma}\right) \tag{1.2}$$

Where **u** is the bulk velocity of the solar wind, **B** is the solar wind magnetic field, **σ** is the conductivity, and **J** is the electric current density (*Gurnett and Bhattacharjee*, 2005). If one assumes that the solar wind plasma is highly conductive, the second term on the right vanishes, causing the magnetic field to be “frozen” into the plasma, or carried by the solar wind bulk velocity. In the solar wind, this “frozen in field” is referred to as the “interplanetary magnetic field” (IMF). When describing the IMF, a coordinate convention known as geocentric solar magnetospheric (GSM) coordinates may be used. In this convention, the origin is the center of the Earth, with the line from Earth to the sun being the x-axis. The z-axis is aligned with Earth’s magnetic dipole axis, while the y-axis is associated with the day-night terminator at a point perpendicular to x and z (*Kivelson and Russell*, 1995). Figure 1.1 shows the rough position of the GSM x- and z-axes in green.

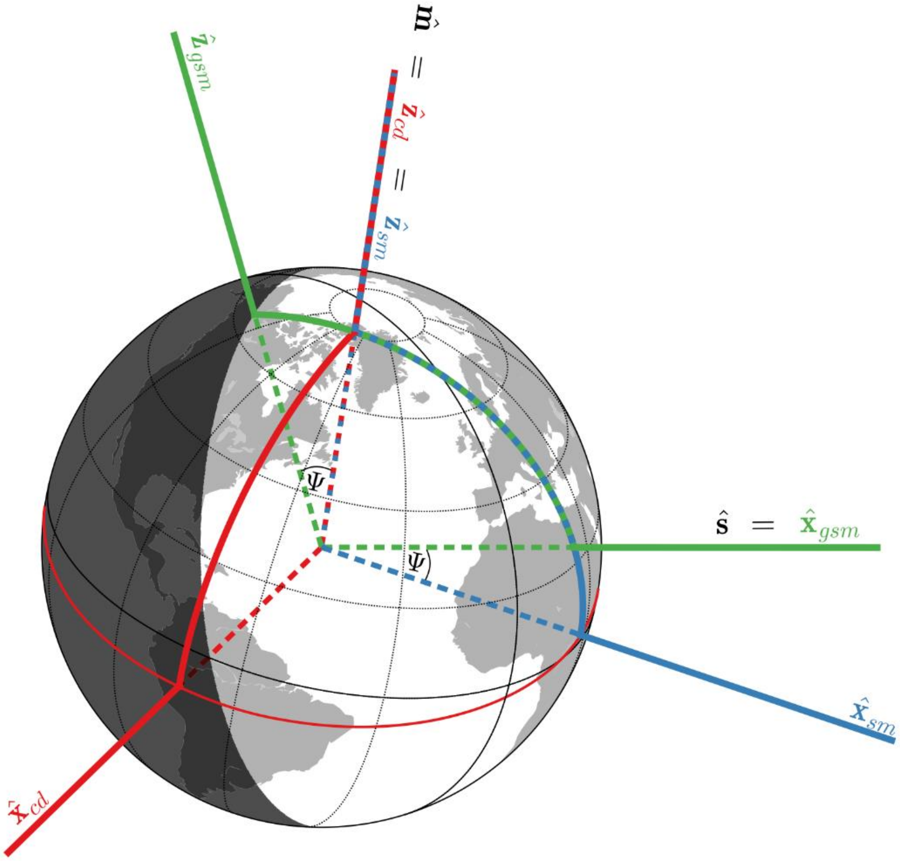

Figure 1.1: Diagram of Magnetic Coordinate Systems (GSM in Green)

(*Laundal and Richmond*, 2017)

Because the sun rotates, the expulsion of plasma is not perfectly radial. The solar wind instead takes on the shape of a spiral, commonly referred to as the “Parker spiral” (*Parker*, 1958). Figure 1.2 shows a standard depiction of the Parker spiral at the scale of Earth’s orbit.

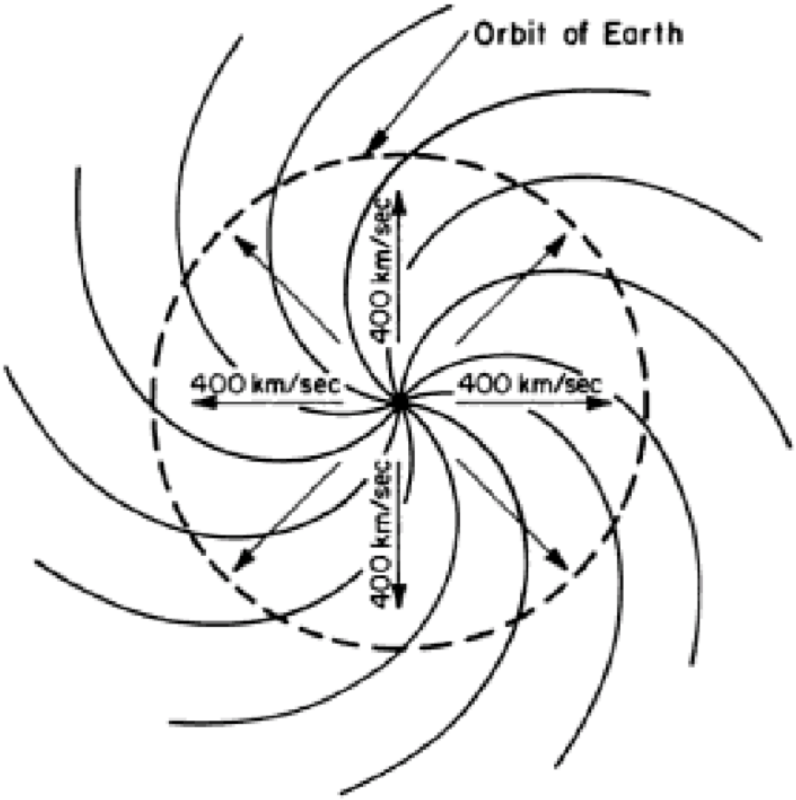

Figure 1.2: A depiction of the Parker Spiral (*Hundhausen*, 1995)

Another noteworthy property of the solar wind is that the flow of plasma from the sun occurs with such speed that the solar wind exceeds the local speed of sound out to radial distances of about 160 AU (*Hundhausen*, 1995). The high speed of the solar wind means that it will create well-defined boundaries whenever encountering an obstacle, known as "shocks." The feature that separates these shocks from those typically found in fluid dynamics is that shocks associated with the solar wind are assumed to be collision-less due to the low density of the solar wind.

1.2 Earth's Magnetosphere

As the solar wind expands outward into interplanetary space, it encounters Earth's magnetic field as an obstacle which exerts an outward magnetic pressure that pushes back against the solar wind bulk flow. This obstruction causes the solar wind to slow down, resulting in the formation of a structure known as the “bow shock.” The shocked solar wind, known as the “magnetosheath,” flows around the Earth’s magnetic field, surrounding it in a cavity of the solar wind flow referred to as Earth’s “magnetosphere.” A diagram of Earth’s magnetosphere and its regions is shown in Figure 1.3 below.

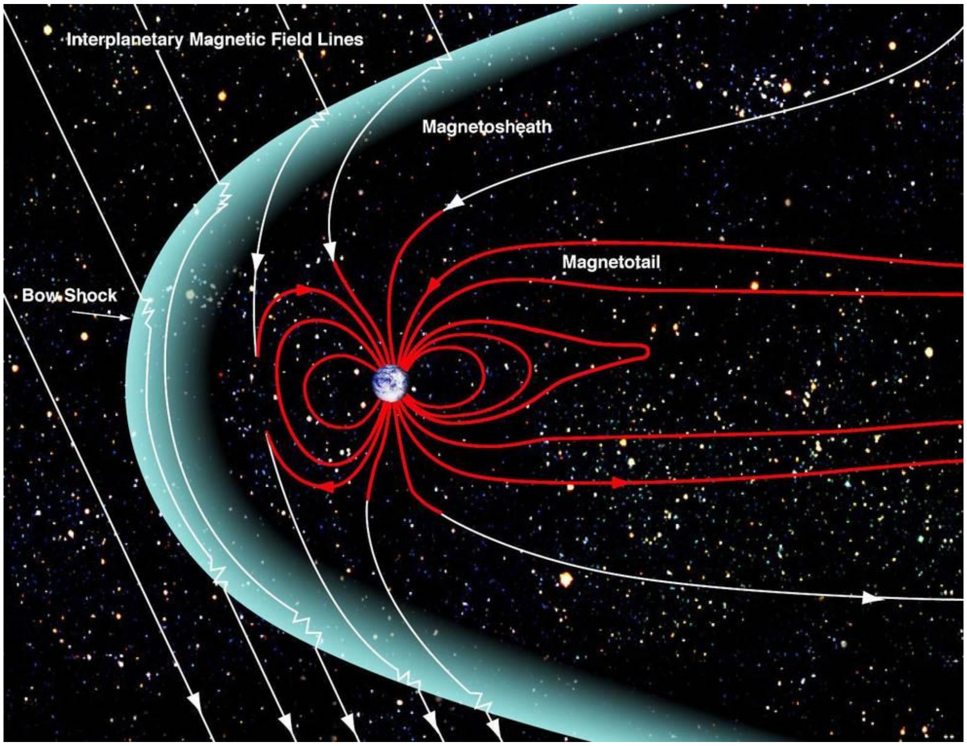

Figure 1.3: NASA diagram depicting the bow shock and magnetosheath (*Kaase,* 2015)

The magnetosphere is heavily compressed on the day side of Earth, forming a long tail (“magnetotail”) on the nightside, with a comet-like appearance (*Walker and Russell,* 1995). The boundary between the shocked solar wind and magnetosphere is referred to as the “magnetopause,” defined as the surface where the dynamic pressure of the solar wind is balanced by the Earth’s magnetic field. Fluctuations in the solar wind speed and density cause the location of both the magnetopause boundary and the bow shock to shift constantly.

Earth's magnetic field at the equatorial dayside is aligned with the positive z-direction in the GSM coordinate system. The alignment of the magnetic field in the IMF, however, is far less constant. As such, there are times when the incoming IMF is at near-opposite orientation to that of Earth's magnetic field when the two collide. This results in a process called "magnetic reconnection," where these opposing field lines merge and reconnect to form new field lines (*Dungey*, 1961). These new field lines are carried over the Earth's polar cap, resulting in additional reconnection at Earth's magnetotail. Depictions of this "Dungey cycle" and its resulting flow pattern in the Earth's ionosphere are pictured in Figures 1.4 and 1.5.

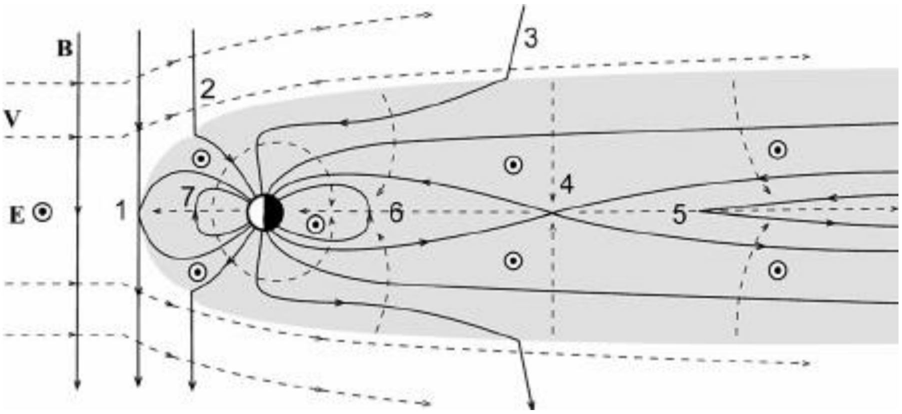

Figure 1.4: A depiction of the Dungey cycle with (1) Magnetic reconnection on the day side, (2, 3) Field lines carrying over the polar cap, and (4, 5, 6) Magnetotail reconnection and subsequent field separation and acceleration. (*Seki et al.*, 2015)

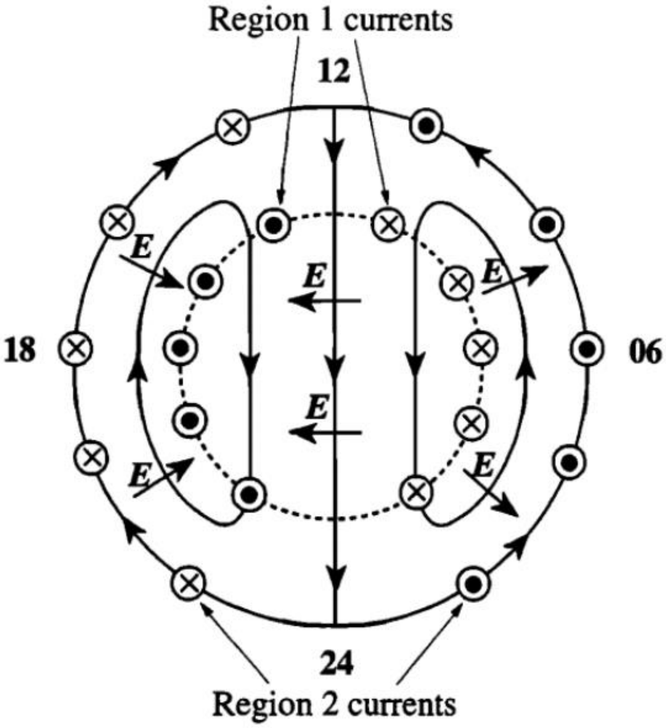

Figure 1.5: The Dungey Cycle mapped onto Earth's Ionosphere. The arrows on the solid lines show the plasma streamlines, and the dashed line shows the open-closed field line boundary (*Cowley*, 2000)

Reconnection is not the only mechanism by which plasma is transported throughout the magnetosphere. As discussed previously, on large scales, the solar wind and magnetosphere can be modeled as a fluid. As such, a contribution to magnetospheric plasma convection can be found in a mechanism known as "viscous-like interactions" (*Axford and Hines*, 1961). This interaction occurs between the solar wind and the magnetospheric boundary. As the incoming solar wind meets the magnetopause, it drags magnetospheric plasma along the magnetopause flanks, resulting in a two-cell ionospheric plasma convection pattern that resembles the structure found in reconnection. Diagrams of these processes are shown in Figure 1.6.

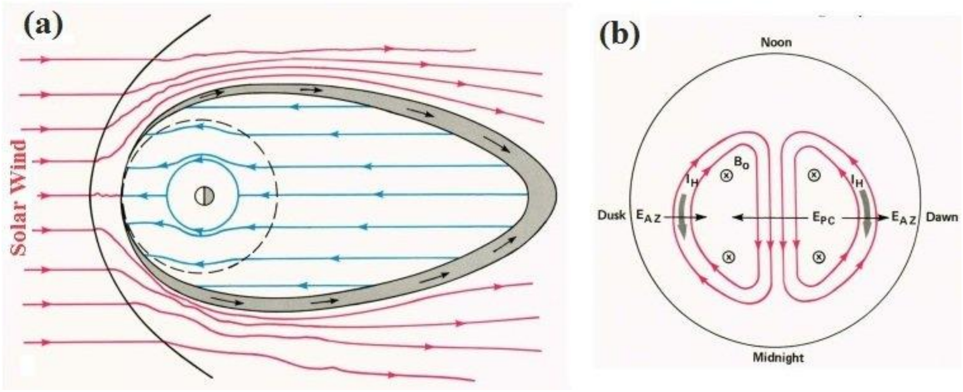

Figure 1.6: (a) Viscous interactions between the magnetosphere and solar wind and (b) Two-cell ionospheric convection pattern (*Singh*, 2019)

1.3 Kelvin-Helmholtz Instabilities

The solar wind and magnetosphere are assumed to be effectively collision-less, so they cannot be truly viscous. The primary candidate for viscous-like interactions is the Kelvin-Helmholtz instability, which has been observed on the magnetopause flanks (*Kavosi and Raeder*, 2015). First documented by *Helmholtz* (1868), the Kelvin-Helmholtz instability (KHI) occurs when two fluids meet at differing velocities parallel to their boundary, known as a “flow shear,” and waves formed on the boundary roll up into vortices. Importantly, MHD fluids are also able to experience the KHI, allowing them to occur in the magnetosphere.

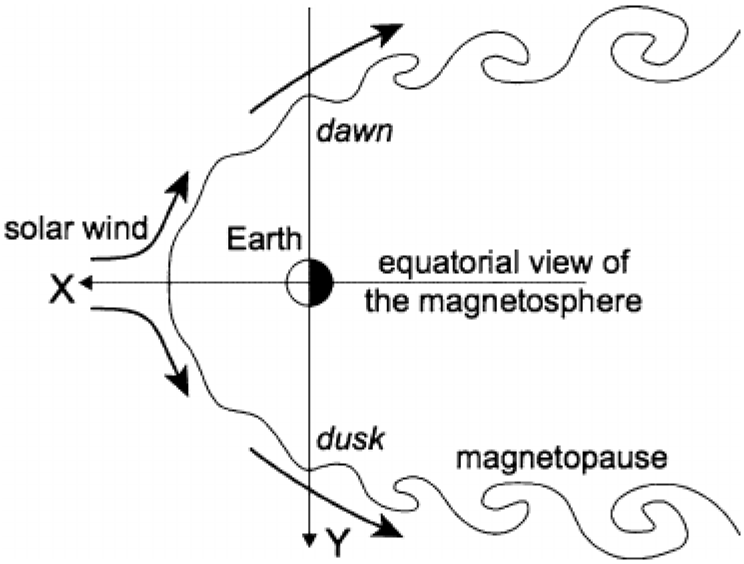

Figure 1.7: A diagram showing a KHI in Earth's Magnetosphere (*Sibeck et al.,* 2014)

One such region of the magnetosphere where the KHI is observed is on the flank of the magnetopause, where the solar wind bulk velocity shears along the boundary, as seen in Figure 1.7. The plasma caught in Earth's magnetosphere is low velocity when compared to the solar wind plasma, making the boundary an excellent candidate for the formation of these KHI events (*Dungey*, 1955). Although the KHI has been observed in the magnetopause (*Kavosi and Raeder*, 2015, and references therein), the detailed dynamics of the plasma within the KHI, as well as how it transports mass and momentum from the solar wind to the magnetosphere, is a topic of ongoing research.

1.4 Solitary Waves

One such topic of on-going research in the KHI is how non-linear kinetic plasma processes play a role in the transfer of mass, energy, and momentum. One such process is the generation of electrostatic solitary waves, which are part of a broader class of phenomena called "time domain structures." When observing a quantity that varies with time, there is a limitation to measurement of multiple properties at once. Notably, a short duration in time removes detailed information in the frequency domain. When phenomena display this property of short time resolution with a broad frequency spectrum, they can be called “time domain structures,” or TDS (*Mozer*, 2015). There have been observations in Earth’s magnetosphere of TDS in the electric field component parallel (E||) to the magnetic field (*Temerin et al.*, 1982). One of the most prominent of these structures, observed by a characteristic unipolar or bipolar electric field, is known as an electrostatic solitary wave, or ESW (*Vasko et al.*, 2017). These ESWs take many forms, potentially resulting from the formation of phase space holes for ions or electrons (*Vasko et al.*, 2017). An example of the electric potential associated with an ESW is shown in Figure 1.8.

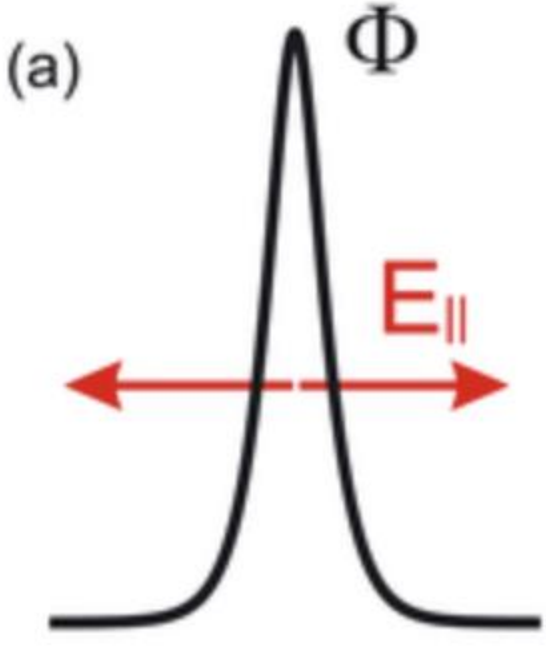

Figure 1.8: Symmetric bipolar divergent parallel electric field (a field which is associated with electron phase space holes) and its associated potential (*Vasko et al.*, 2017)

An electron phase space hole results in a “pseudo-particle” spike in the electrostatic potential, where an absence of electrons creates a local increase of detected positive charge. The mechanism by which this phase space hole is created can be described using the kinetic theory of plasmas. This is done by assuming that the phase-space distribution function experiences different behavior depending on the value of the potential compared to the square of the bulk velocity (*Muschietti et al.*, 1999). In short, if the kinetic energy of an electron is not sufficient to overcome the potential, it becomes trapped. As such, one may define two separate electron distribution functions: a “trapped” distribution (f_t) and a freely passing distribution (f_e):

$$f_t(w) = \frac{6+\left(\sqrt{2}+\sqrt{-w}\right)(1-w)\sqrt{-w}}{\pi\left(\sqrt{2}+\sqrt{-w}\right)(4-2w+w^2)} + \frac{2\sqrt{-w}}{\pi\delta^2}\left[1+2\ln\left(\frac{\psi}{-4w}\right)\right] \tag{1.3}$$

$$f_e(w) = \frac{6\sqrt{2}}{\pi(8+w^3)} \tag{1.4}$$

Where $w = v^2 - \psi$ is our normalized energy, $\phi(x) = \psi \exp(-0.5x^2/\delta^2)$ is the electrostatic potential expressed as a Gaussian of amplitude ψ and width δ, and f_t and f_e are evaluated for $w<0$ and $w>0$ respectively (*Muschietti et al.*, 1999). The shape of the resulting distribution shows a plateau with a dip in its surface centered around zero-velocity and the origin. The presence of the gaussian potential has produced a phase space hole for electrons. Figure 1.9 shows the resultant distribution function from the above calculations.

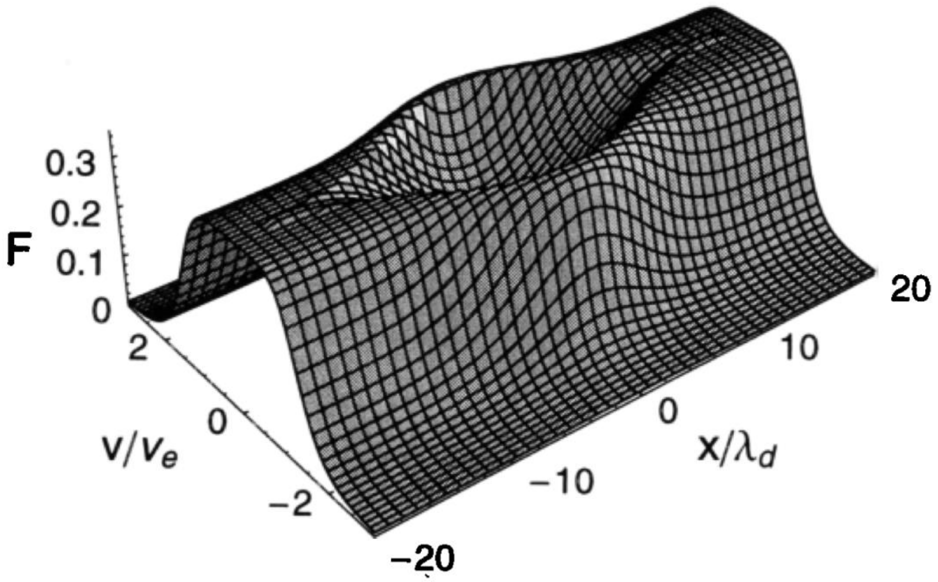

Figure 1.9: Plot of the distribution functions in Equations 1.3 and 1.4. Note the descent in the center of the distribution as the electron phase space hole. (*Muschietti et al.*, 1999)

Electron phase space holes form as the potential of a growing wave or instability approaches the electron kinetic energy, allowing a portion of the population to become trapped. A common instability associated with growing waves is a current driven instability (*Buneman*, 1963). As such, one might expect to see an increase in the counts of ESWs when a satellite encounters a boundary with large current, which is precisely what is observed (*Hansel et al*., 2021). Figure 1.10 shows the occurrence of ESWs at various positions relative to Earth's magnetosphere, with an increased occurrence near the bow shock and magnetopause.

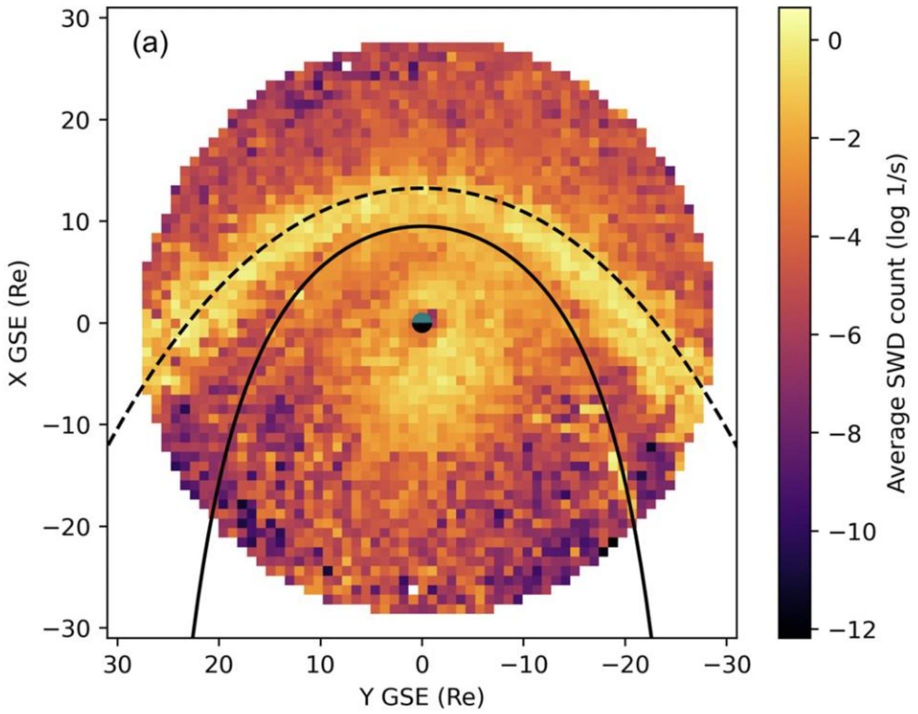

Figure 1.10: Occurrence of 3-12 mV/m ESWs by position (in GSE coordinates). Note the increased concentration surrounding the bow shock (dashed) and the magnetopause (solid). (*Hansel et al*., 2021)

The presence of these ESWs can be used as a marker for the presence of non-linear kinetic instabilities. This can therefore identify the presence of strong wave-particle interactions within larger scale magnetospheric phenomena, including the KHI.

1.5 Motivation

Solitary waves are a fascinating phenomenon of great use to the study of instabilities. The extremely short timescale of these events, along with their location in the magnetosphere, leads to difficulties in observation. However, as shown previously (*Hansel et al.*, 2021), solitary waves can prove to be incredibly useful for identifying kinetic instabilities in Earth's magnetosphere.

This study is motivated as a continuation of *Wilder et al.* [2021]. The previous study was conducted on 3 KHI events and observed their occurrence of ESWs. The study observed that the presence of ESWs appeared to decrease as an event was measured further down-tail. The study also observed that the presence of ESWs seemed to coincide with large magnetic fluctuations normal to the magnetopause and high field-aligned currents. The current study seeks to include a larger range of events to observe how ESW occurrence compares with the hypothesis of reduced down-tail observation, while simultaneously observing the relations between ESW occurrence and various solar wind properties. This study also seeks to evaluate a hypothesis that the presence of ESWs affects the local plasma by modifying the temperature. This can provide information on what drives non-linear kinetic activity in the KHI, as well as what effect it may have on the local plasma.

METHODOLOGY

To characterize the magnetosphere and solar wind during KHI events, in-situ satellite observations are used. For this study, a list of events compiled by *Wilder et al.* (2023, submitted) for studying reconnection in KHIs was used, and data surrounding the events was collected from NASA's OMNI database and the Magnetospheric Multiscale mission. Data collected from OMNI was primarily used for analysis of solar wind properties, while MMS data was used to obtain data about the local magnetospheric conditions, location of the KHI observations, and the distribution of TDS within the boundary layer during the KHI.

2.1 NASA OMNI Database

NASA has launched multiple spacecraft capable of measuring the IMF and solar wind in the vicinity of Earth's magnetosphere. There has been a continuous effort to consolidate and process data from them, taking measurements and propagating them to the same location (~17 Earth radii [R_e]) based on the observed solar wind conditions and estimated time of arrival at

Earth, allowing for a detailed database about solar wind conditions near Earth's bow shock nose. This database is called "OMNI" and serves as the primary resource used in this study for describing solar wind conditions near Earth (*King and Papitashvili*, 2023).

The database is split into two categories based on temporal resolution: Low-resolution OMNI (LRO) data and High-resolution OMNI (HRO) data. The LRO data is averaged across an hour timespan, with data from the ACE spacecraft being normalized against the Wind spacecraft observations (*King and Papitashvili*, 2005). The HRO data consists of 1-minute and 5-minute resolutions, with data being collected from the ACE, Wind, IMP 8, and Geotail spacecraft (K*ing and Papitashvili*, 2023). In both resolutions, data is collected for the IMF bulk velocity, number density, magnetic field vectors, electric field vectors, plasma temperature, and plasma pressure. This project uses averages of 5-minute OMNI-HRO to characterize the average solar wind conditions during each KHI event.

2.2 The Magnetospheric Multiscale Mission

The Magnetospheric Multiscale (MMS) mission consists of four spacecraft designed to observe kinetic-scale processes in the Earth's magnetosphere; more specifically, MMS is designed to observe magnetic reconnection, turbulence, and particle acceleration. During the primary phase of the mission, the objective of MMS was to understand reconnection at Earth's magnetospheric boundaries (*Burch and Torbert*, 2015). Some of the phenomena MMS was designed to explore - such as electron-scale reconnection - required detailed time resolution on small spatial scales, requiring the spacecraft to have the ability to reduce their separation to as small as 7 km apart. The MMS mission has two primary configurations it takes on: tetrahedral and a "string of pearls." The tetrahedral formation (shown in Figure 2.1) allows for MMS to collect data in 3 dimensions, with offset spacecraft positions allowing for accurate calculation of gradients down to the electron scale.

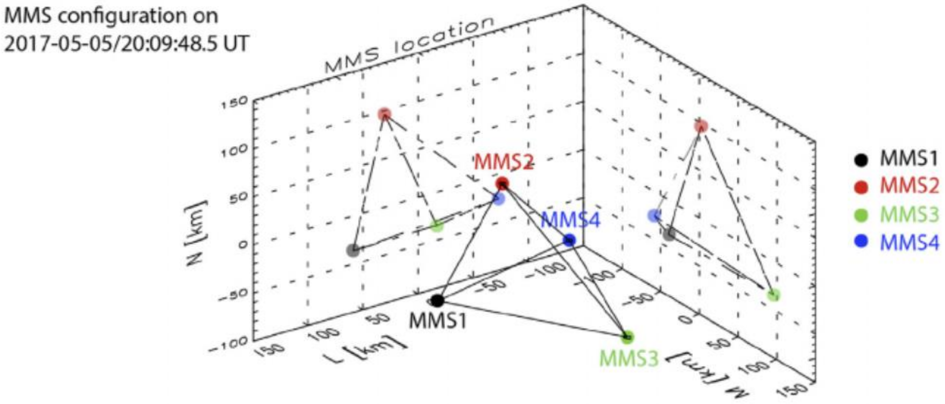

Figure 2.1: An example of the MMS tetrahedral formation (*Hwang et al.*, 2021)

The string of pearls, where the spacecraft simply follow a similar orbit in a single-file line, allows for more information about extended time scales: as the four spacecraft pass through roughly the same orbit, their readings can be compared to see if certain magnetospheric measurements remain constant at the same location, giving a rough time evolution for a location in the magnetosphere. However, this formation of MMS is typically reserved for targeted scientific campaigns, and the mission is typically in the tetrahedral configuration. All events used in this study occurred when MMS was in a tetrahedral configuration.

This study will express MMS data using the Geocentric Solar Ecliptic (GSE) coordinate system instead of the previously discussed GSM coordinates. In GSE coordinates, the x-axis is still defined as the line pointing towards the sun from Earth's center, but the z-axis is defined as perpendicular to the Earth's orbit around the sun, with the y-axis being perpendicular to both, such that it forms a right-handed system (*Hapgood*, 1992). Figure 2.2 shows a depiction of the GSE coordinate system.

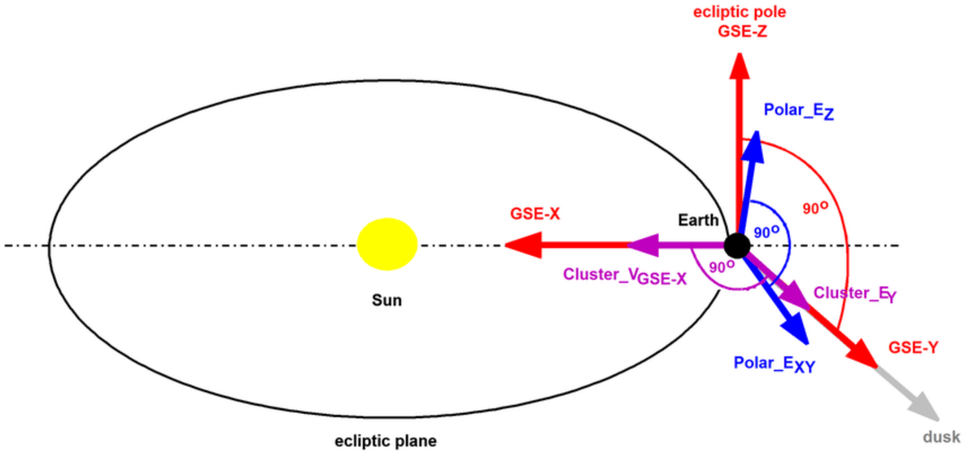

Figure 2.2: Diagram of the GSE coordinate system. Note that the z-axis is aligned with the ecliptic pole rather than the Earth's magnetic pole. (*Horvath and Lovell*, 2019)

Each MMS spacecraft contains a wide suite of instruments that measure local plasma conditions, but this study will focus on three primary instruments: Fast Plasma Investigation (FPI), the Fluxgate Magnetometers (FGM), and the Solitary Wave Detector (SWD) from the MMS Electric Field Double Probes (EDP) and Digital Signal Processor (DSP).

2.2.1 Fast Plasma Investigation

FPI was designed to measure the directional flux of ions and electrons in the magnetosphere, with enough time resolution to observe small-scale plasma dynamics (*Pollock et al.*, 2016). To accomplish this, each spacecraft uses 8 top hat spectrometers, 4 each for ions and electrons, allowing for a complete field-of-view for spectroscopy (*Pollock et al.*, 2016). These spectrometers have unique geometries applied to them depending on their intended particle and are designated Dual Electron Spectrometers (DES) or Dual Ion Spectrometers (DIS). The counts registered by these spectrometers can be used to calculate a velocity distribution function, as the counts observed by each of the spectrometers' 16 pixels can be expressed by the following:

$$C_{ij}^{O} = \tau\sigma_j \int_{v-} d^3\, v\left(N_j \cdot v\right) f(x', v', t) R_{ij}(v') \tag{1.5}$$

Where C denotes the counts detected across accumulation time τ by section "*i"* when only aperture σ_j is lit, N_j is the unit normal vector pointing out from said aperture, and R_{ij} is an experimentally determined response matrix between the pixels associated with "i" and "j" (*Pollock et al.*, 2016). Using certain limits and assumptions, (1.5) can be used to determine a velocity distribution function, the moments of which can be calculated to obtain number density, bulk flow velocity, pressure tensor elements, and the heat-flux vector (*Pollock et al.*, 2016).

2.2.2 Fluxgate Magnetometers

The FGM is a collection of two separate types of magnetometers: an Analog Fluxgate magnetometer (AFG) and a Digital Fluxgate magnetometer (DFG) (*Russell et al.*, 2016). Both magnetometers bear the same sensor design, two perpendicular magnetic rings with both a driving set of wire windings and a detecting set of wire windings (*Russell et al.*, 2016).

The primary difference between these two magnetometers is the design of their respective circuits. The exact design behind these circuits is beyond the scope of relevance to this discussion, but the purpose behind the different designs was expressly to ensure redundancy and accuracy for the measurements collected (*Russell et al.*, 2016). The relevant data collected from these instruments are the magnetic field vectors observed by each of the spacecraft, as well as some rudimentary data about the spacecraft position, though the latter is often used for calculation rather than directly for its positional information. Rudimentary calculations allow this magnetic field data to be processed into either GSE or GSM coordinates, with the x-, y-, and z-components being separated in each.

2.2.3 Electric Field Double Probes

The EDP is a blanket term describing both the two Spin-Plane Double Probes (SDP) and the Axial Double Probe (ADP) found in MMS. By combining the data from the three double probes, a 3D measurement of the electric field vector at the spacecraft is found. While each of these EDPs has its own unique properties, the general design requirements of a double probe are consistent. A double probe consists of two booms that extend from the spacecraft in opposite directions, with a probe attached to the end of each. A bias current is applied to each probe, allowing it to remain at the ambient plasma potential (*Lindqvist et al.*, 2016). The use of a double probe design also allows the probes to collect data about the potential difference along their axis, which can determine the electric field vector (*Pedersen et al.*, 2008).

The SDP consists of two double probes, for a total of four probes separated by right angles from each other in the plane of spacecraft rotation. The placement of these probes is depicted in Figure 2.3, and a more detailed diagram of the SDP instrumentation is shown in Figure 2.4.

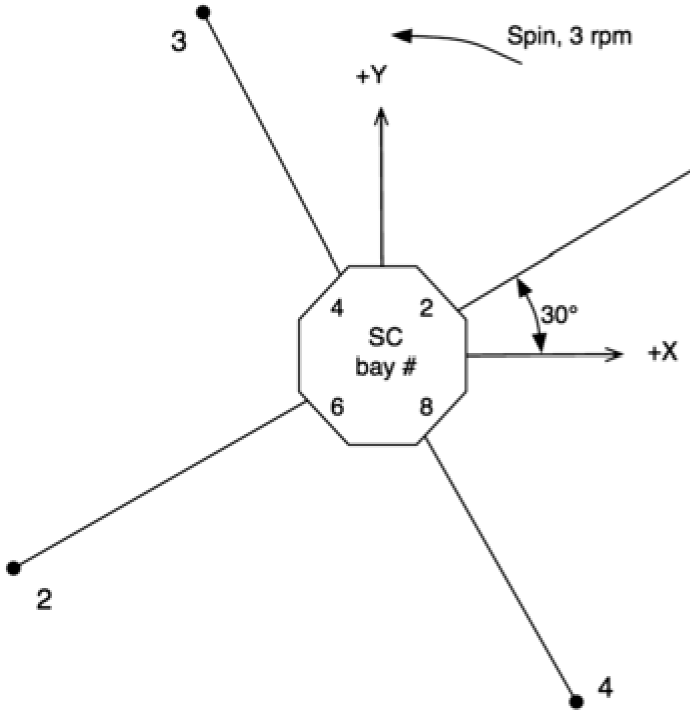

Figure 2.3: Spin-Plane Double Probe booms and probes (*Lindqvist et al.*, 2016)

The ADP consists of a single double probe on the axis of rotation for the spacecraft but includes a separate receiving element (RE) at the end of each boom (*Ergun et al.*, 2014). Some adjustments to the design of the ADP were necessary because of the SDP design: the ADP needs to account for the rotation of the spacecraft, and the booms that make up the ADP need to be slightly different lengths to account for the axial offset of the SDP (*Ergun et al.*, 2014).

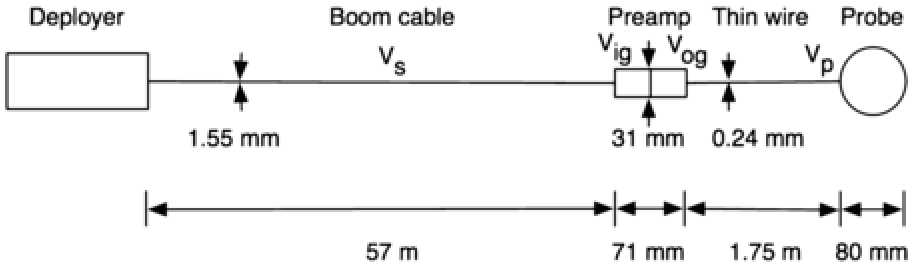

Figure 2.4: Schematic of instrumentation for the SDP, with Spacecraft Potentials (V) (*Lindqvist et al.*, 2016)

2.2.4 Digital Signal Processor and Solitary Wave Detector

The DSP is used within MMS to process data from the EDPs and search coil magnetometers (*Ergun et al.*, 2014). However, the limited volume of data retrievable from MMS necessitates the DSP to be selective about its chosen algorithms. At present, the DSP consists of five primary processes: broadband filters, waveform filters, power spectra processing, high-speed burst memory, and solitary structure detection (*Ergun et al*., 2014). Each of the datasets created from these processes is useful to MMS, but this project makes special use of the resultant data from the solitary structure detection.

One such algorithm on the DSP that is vital to the current study is the solitary wave detector (SWD), which is designed to detect TDS. The SWD analyzes data across adjustable millisecond time scale windows, collecting individual data points from a single SDP pair. From there, the SWD calculates the average electric field across the window, as well as a custom variation function:

$$\sigma_{est} = \langle |x(1:n)| \rangle \tag{1.6}$$

where x is the set of all n data points in the window. This custom variation is then compared to the peak value of |x|. If the peak |x| is greater than four times the custom variation, the window is flagged as a solitary structure (*Ergun et al.*, 2014). The SWD places each flagged window into one of four “bins” separated by amplitude. Bin 1 includes all flagged events with a peak amplitude less than 3 mV/m, bin 2 includes flagged events between 3 and 12 mV/m, bin 3 includes events between 12 and 50 mV/m, and bin 4 includes all flagged events with a peak amplitude higher than 50 mV/m (*Hansel et al.*, 2021). When tested on data from the NASA THEMIS mission, electron phase space holes produced an approximately 30% false negative rate and 10% false positive rate in the SWD (*Ergun et al.*, 2014). However, this produces accurate enough detection for use in statistical studies of the prevalence of TDS.

2.3 Identification of KHI Events

Since the current project focuses on KHI events, correctly identifying them in satellite data is of great importance. As mentioned earlier, we use the events identified by *Wilder et al.* (2023, submitted). Since the identification of those events was integral to this project, we will summarize the selection procedure here. As the KHI is a periodic phenomenon that occurs over a large time duration and between two regions of differing plasma characteristics, it has a distinct appearance in the data. KHI can be identified by a repeated periodic crossing between these two different plasma regions, most visually obvious in the energy spectra data as shown in Figure 2.5. On the left of Figure 2.5, the spacecraft is in the magnetosphere, and on the right it is in the magnetosheath. Shortly after 9:15 UT, the observed spectra begin oscillating between magnetosphere-like and magnetosheath-like conditions. This periodic crossing also coincides with similar oscillations in temperature and number density. Additionally, there are reversals in the magnetic field components normal to the magnetopause (B_x and B_y) as the spacecraft traverses between magnetosphere-like plasma and magnetosheath-like plasma. These features are consistent with KHI events and are used in the present study (*Wilder et al.*, 2021). Additionally, only events where observations of the KHI lasted at least 30 minutes and the highest resolution “burst” data from MMS was transmitted to the ground were used for this study.

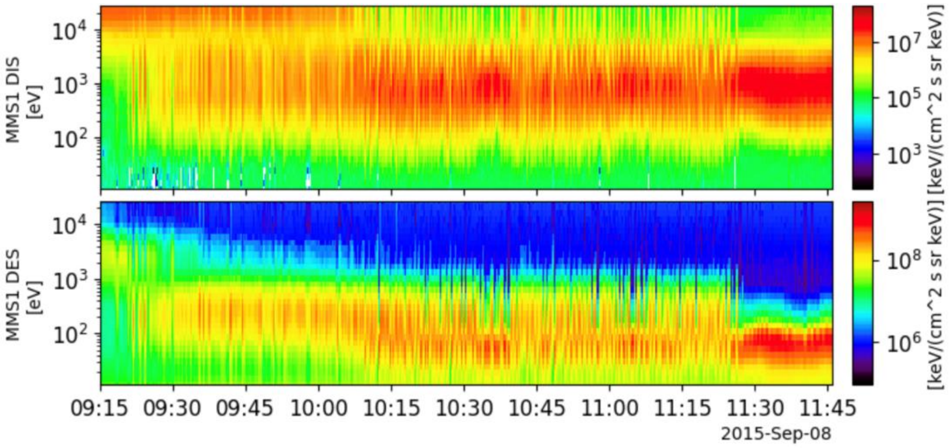

Figure 2.5: An example of plasma region crossing observed in energy spectra. Pictured is the ion and electron omni-directional energy spectra for the KHI which occurred September 8, 2015.

RESULTS AND DISCUSSION

Using the criteria above, 15 candidate KHI events were identified, and the relevant data collected. Figure 3.1 displays one of these events as an example, and the summary plots for the remaining events can be found in Appendix A. The first 2 panels of Figure 3.1 display the same type of data as shown in Figure 2.5. Below these, Figure 3.1 displays ion and electron temperature based on orientation relative to the magnetic field vector. Following this, the figure then displays ion and electron number density, the velocity of the plasma in GSE coordinates, the components and magnitude of the magnetic field vector in GSE, a calculated value of temperature anisotropy, and solitary wave data counts. As expected, these events display the periodic fluctuations in the conditions described above: all temperatures, number densities, the velocity components, and magnetic field vector components varied in similar intervals to the observed pattern in the energy spectra. From Figure 3.1, it was also observed that the temperature anisotropy, although significantly less pronounced, also appeared to change periodically with the KHI. Interestingly, the KHI events consistently show the presence of Bin 1 solitary waves, but rarely any of the other bins. As such, most of the following analysis involving solitary waves will focus only on the Bin 1 data.

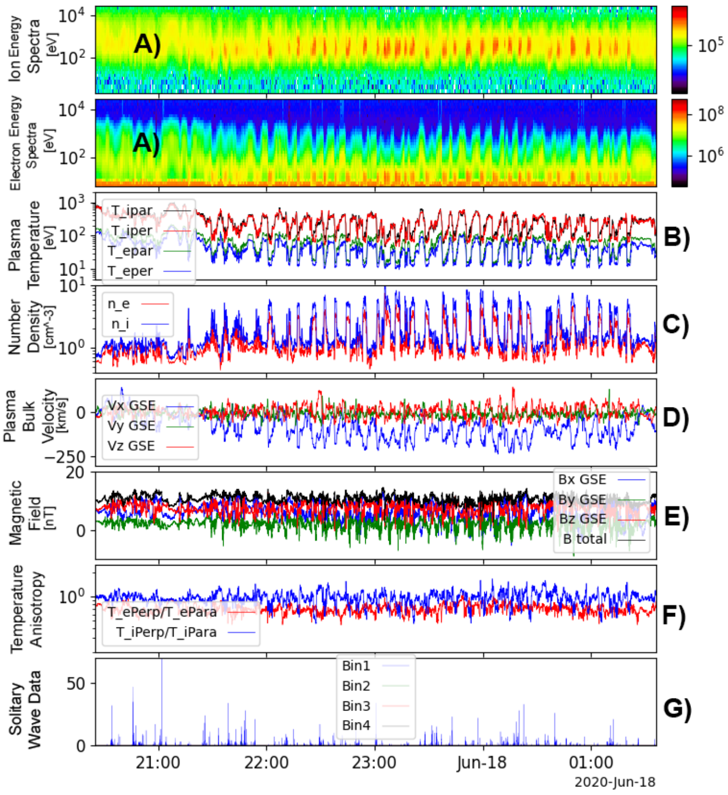

Figure 3.1: A plotted KHI event, including (from top to bottom) (A) Ion and Electron Omni-directional Energy Spectra, (B) Ion and Electron Temperature, separated by Magnetic Field Orientation, (C) Ion and Electron Number Density, (D) Bulk velocity in GSE coordinates, (E) Magnetic Field Vector Components, (F) Perpendicular vs Parallel Temperature Ratios for Ions and Electrons, (G) Solitary Wave Data counts

3.1 Temperature Isotropy and Solitary Waves

The first portion of this data that was investigated by this study was the temperature anisotropy for ions and electrons, and more specifically how those values correlated to SWD data. Previous studies have suggested that ESWs may act to thermalize the local particle populations, influencing them into isotropy (*Khotyaintsev et al.*, 2017). To investigate this, for each of the selected KHI events, the data for temperature anisotropy (in both ions and electrons) and solitary wave count were extracted. Since the data were collected at different sampling rates, they were interpolated to the same time cadence, and were then plotted against each other. From the plots of this data, there were peaks in the solitary wave data as a function of temperature anisotropy at single values, so a function was developed to determine the location of each peak:

$$\frac{(r_t \cdot x_{SW})}{\bar{x}_{SW} s_t} \tag{3.1}$$

Where r_t is the temperature isotropies expressed as a ratio of perpendicular to parallel (with respect to the magnetic field), x_{SW} is the solitary wave counts, and S_t is the number of datapoints used. This formula was found to be quite faithful in reproducing the peaks seen in the events where a peak was easily visually identified and was applied to events with less obvious peaks. Finally, with the mean of the solitary wave count, bars of one standard deviation (adjusted for the skew factor) were plotted for each event. Figure 3.2 shows a scatterplot of the May 20, 2019 KHI, with ion temperature anisotropies (blue) and electron temperature anisotropies (red) plotted against the sampling-adjusted Bin 1 SWD. The plots for the remaining events are in Appendix B. The peak function described above produced the temperature ratios for ions (orange) and electrons (green) associated with the peak of each dataset.

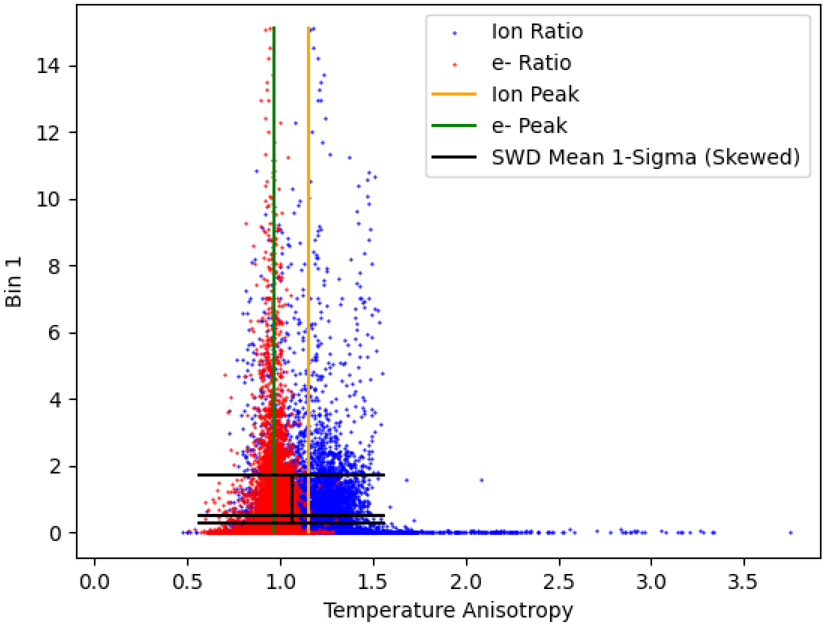

Figure 3.2: Plot of Bin 1 Solitary Wave counts as a function of Electron (red) or Ion (Blue) Temperature Anisotropies, with included Peak function and Solitary Wave concentration. Event from May 20, 2019

The findings from these plots show a consistent pattern where the electron temperature ratio at which there is a solitary peak is slightly parallel ($\overline{r}_{t_e} = 0.86$) while the ion ratio is isotropic to slightly perpendicular ($\overline{r}_{t_i} = 1.09$). Doing a rough average of these two values shows near isotropy as the peak for the whole plasma, factoring in the similar number densities observed ($\overline{r}_t = 0.97$). Unsurprisingly, the overall standard deviation of the solitary wave data appears dominated by the pronouncement of this peak, with more pronounced solitary wave peaks resulting in a higher standard deviation. Since the KHI events occur across a large timescale while the solitary waves occur as inconsistent bursts, many of the recorded points for the temperature anisotropy graph have a SWD count of 0, causing the graphs to be heavily skewed (especially in cases with pronounced peaks containing few data points).

The findings imply that the ESWs influence the temperature anisotropies of ions and electrons, driving ions to become more isotropic while driving electron temperature to become highly parallel to the magnetic field vector. Since this suggests that ESWs can impact local plasma conditions within the KHI, it was deemed worthwhile to attempt to observe how the solar wind data, event location, and previously collected data contributed to the creation of these ESWs.

3.2 Occurrence of Solitary Waves in KHI

The next portion of this study involved correlating the occurrence rate of TDS with various parameters relating to the solar wind as well as the spacecraft position along the magnetospheric flanks. Certain OMNI data and related variables were unavailable for two events, and so they could only be analyzed for their event locations, with the remaining 13 being used for solar wind data analysis. More specifically, the OMNI data available for the April 18, 2018 event has large missing values for the solar wind velocity, while the December 4, 2021 event had missing data for pressure, bulk velocity, and electric field components. In addition to the OMNI variables, a separate calculated variable, called the "reconnection ratio" was used (*Wilder et al.*, 2023, submitted). The process for calculating this value was to identify compressed current sheets that flank vortices in the KHI, signified by sharp reversals in magnetic field component normal to the magnetopause and a sudden transition from magnetosphere-like to magnetosheath-like plasma (*Sonnerup and Scheible*, 1998). The "Walén test" was then performed on each to identify which current sheets exhibited evidence of reconnection ion outflows (*Paschmann et al.*, 1986). The percentage of the compressed current sheets that exhibited evidence of reconnection was called the "reconnection ratio." Scatter plots between average SWD counts and each analyzed variable can be found in Appendix C.

In the section to follow, this study discusses results using the collected data. The parameters taken for the following results were averaged across the duration of the event (including spacecraft position, which remains relatively constant near spacecraft apogee). Following this, the relations between each parameter and the average SWD counts were analyzed with standard p-values and R-squared values used for a linear regression, which allow for determination of the accuracy of a linear fit to the behavior of a phenomena. R-squared values show the proportion of variance in a data set that can be explained by the regression applied to it, so the closer to 1 the value is, the better a fit is for the data. The p-value is used to denote the chance that the chosen relation could have arisen from random noise rather than an actual pattern, with values closer to 0 producing a more rigorous conclusion of correlation. These statistics are heavily favored for linear regressions, but analysis in the background using similar parameters for non-linear regressions found comparable results (not shown). For the purposes of this study, a standard p-value of 0.05 (5% chance of no relation) was used as a cutoff value for significance.

First, a linear regression was taken on the GSE position of the spacecraft when compared to the average solitary wave occurrence across the event. This regression appears to correlate heavily with the GSE x-coordinate ($p = 0.0015$, positive correlation), the absolute value of the GSE y-coordinate ($p = 4.9 \cdot 10^{-6}$, negative correlation), and the GSE z-coordinate ($p = 0.018$, negative correlation). The R-squared value for the x-coordinate ($R^2 = 0.552$) and z-coordinate ($R^2 = 0.359$) suggest that, while significant, they are insufficient to explain the variance in the data. The R-squared for the absolute y-coordinate ($R^2 = 0.810$), however, suggests a much stronger dependence. Figure 3.3 below depicts the relationship between the KHI average GSE y-coordinate and the event-averaged SWD count.

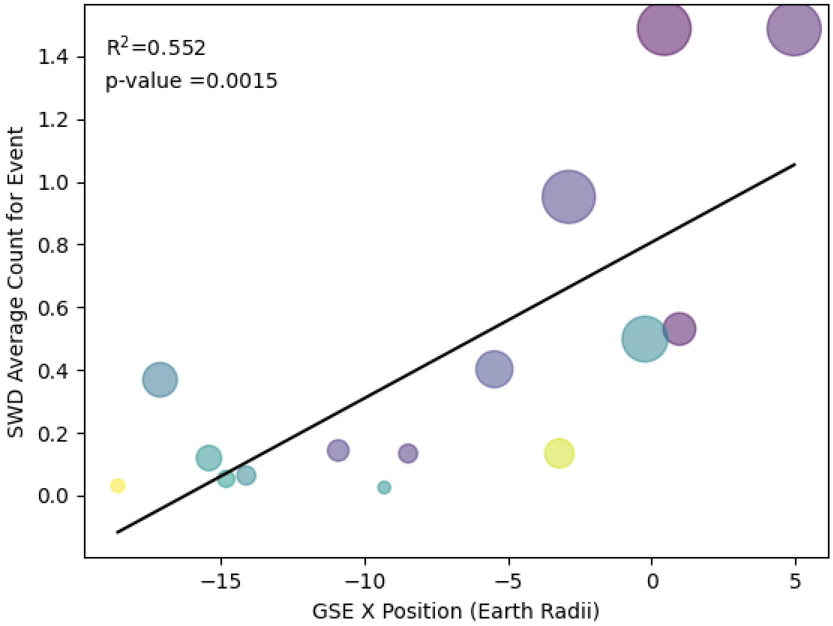
R^2=0.552
p-value =0.0015
SWD Average Count for Event
1.4
1.2
1.0
0.8
0.6
0.4
0.2
0.0
−15
−10
−5
0
5
GSE X Position (Earth Radii)

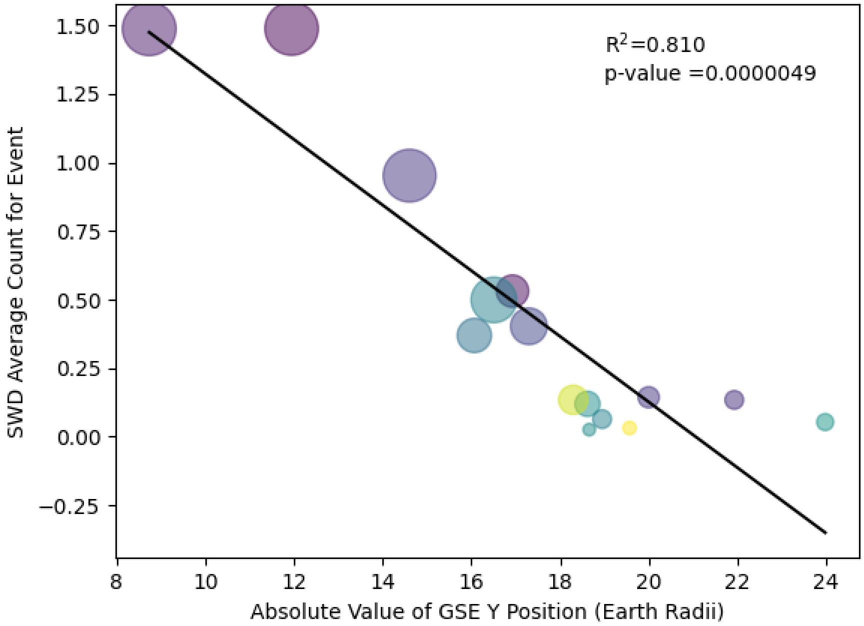
R^2=0.810
p-value =0.0000049
SWD Average Count for Event
1.50
1.25
1.00
0.75
0.50
0.25
0.00
−0.25
8
10
12
14
16
18
20
22
24
Absolute Value of GSE Y Position (Earth Radii)

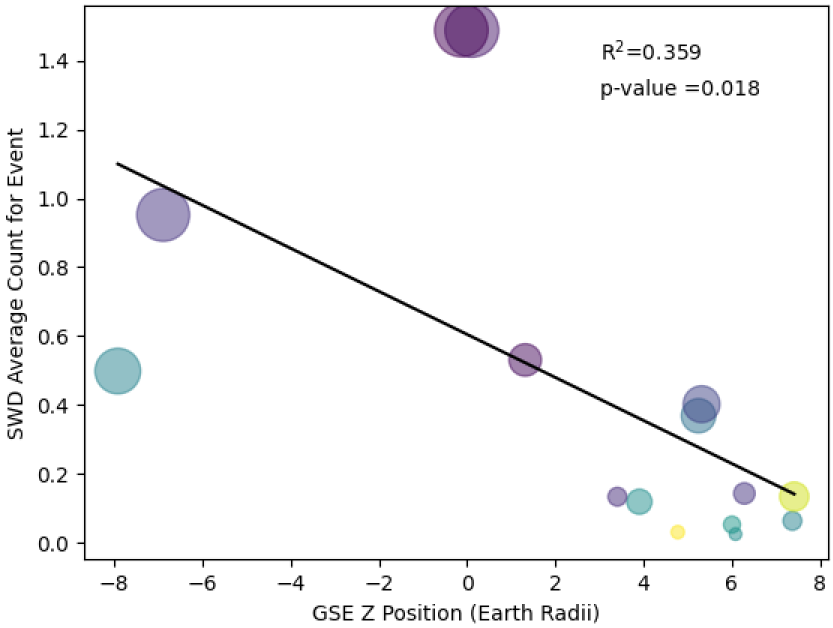

Figure 3.3: Comparison of average Solitary Wave count and GSE x-, y-, and z-coordinates of KHI. A larger dot indicates a higher standard deviation, and a more yellow dot indicates a higher skew.

Using 5-minute averages from OMNI data, comparisons were made between the average SWD counts and the solar wind velocity, magnetic and electric fields, temperature, pressure, and number density. In addition to these, the previously discussed reconnection ratio metric was used. Reconnection ratio showed an unexpectedly mild correlation ($p = 0.014$, $R^2 = 0.439$). Of the remaining parameters, only solar wind temperature ($p = 0.067$) and number density ($p = 0.271$) showed p-values greater than 0.05, suggesting possible correlation for all the other variables. From these, solar wind velocity ($R^2 = 0.516$, positive correlation) and pressure ($R^2 = 0.610$, positive correlation) showed the strongest correlation. Figure 3.4 shows the relationship between the KHI average solar wind pressure and the event-averaged SWD count. Table 3.1 is a table which shows the results of the linear fit for each parameter tested.

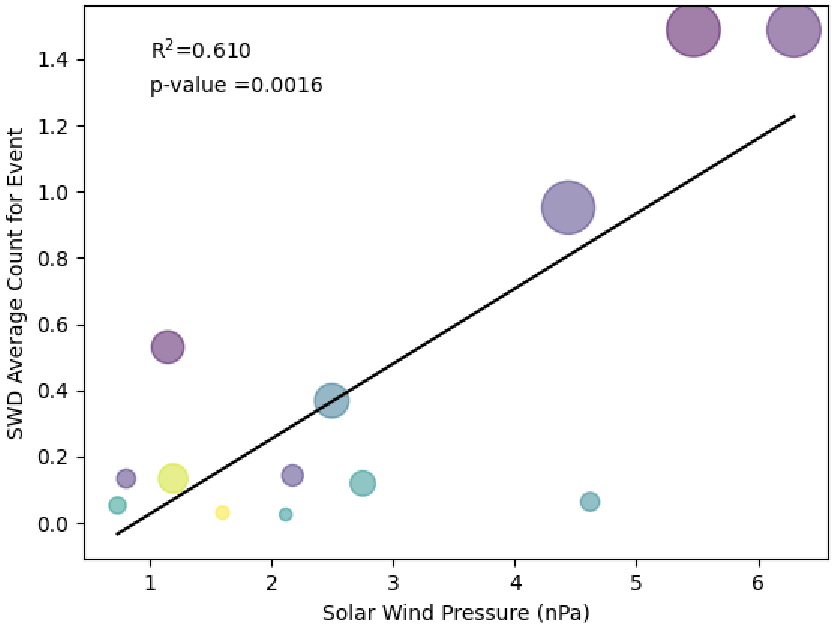

Figure 3.4 Comparison of average Solitary Wave count and OMNI Solar Wind Pressure Data. A larger dot indicates a higher standard deviation, and a more yellow dot indicates a higher skew.

Parameter	**Statistics of Linear Fit**
GSE x-coordinate	R^2=0.552 p=0.0015
Absolute value of GSE y-coordinate	R^2=0.810 $p=4.9 * 10^{-6}$
GSE z-coordinate	R^2=0.359 p=0.018
Reconnection ratio	R^2=0.439 p=0.014
Solar wind bulk velocity	R^2=0.516 p=0.0057
Solar wind B_z	R^2=0.343 p=0.035
Solar wind electric field magnitude	R^2=0.380 p=0.025

Solar wind temperature	R^2=0.274 p=0.067
Solar wind pressure	R^2=0.610 p=0.0016
Solar wind number density	R^2=0.109 p=0.271

Table 3.1: A table comparing the parameters of this experiment to their R-squared and p-values for the linear regression applied to each against ESW occurrence

3.3 Discussion

That the occurrence of solitary waves in KHI is dependent on the location of the event can be explained by the following: the KHI vortices expand as they move along the flanks of the magnetopause, with the scale size increasing, turbulence relaxing, and the associated currents dissipating. This changing structure could easily result in the observed changes to the solitary wave counts. One notable observation is that while the solitary wave occurrence appears asymmetric in the axis of its ecliptic pole. This study has determined two potential causes for this asymmetry. First, there were only 3 events in the negative GSE z-domain: a lack of data which may cause outliers to hide a true symmetry. Secondly, though not fully aligned, the GSE z-axis is adjacent enough to Earth’s magnetic axis that the asymmetric solitary wave data may be a byproduct of the KHI’s interaction with Earth’s magnetic field.

The regressions formed from the solar wind parameters require more involved explanations. Given that the occurrence of solitary waves is associated with turbulence, the results suggest that an increase in solar wind velocity and pressure may result in a more turbulent KHI, leading to increased ESW occurrence. The observation of KHI has established that the vortices preserve the internal conditions of the two interacting fluids decently. As such, the solar wind velocity and pressure might also contribute to the KHI in determining vortex frequency and shape. If the shape and number of vortices involved in a KHI play a significant role in the formation of solitary waves, this may be an additional explanation for their positive correlation.

This study finds that the previous study by Wilder et al. (2021) was partially correct in the hypothesis that KHI experience fewer TDS as they propagate down-tail, but that it may be more accurate to say that there is a reduced occurrence of TDS as the KHI propagates along the flanks and away from local noon. This study further identifies a potential association between TDS occurrence and solar wind velocity and pressure. While the other observed solar wind conditions implied some connection to the occurrence of TDS, there was no substantial evidence that any of the conditions were largely responsible for (or a result of) the TDS. Similarly, the reconnection ratio, while seemingly connected to the number of TDS, did not show adequate explanation of variance to be considered a primary factor. This result is surprising, as many studies have shown the presence of solitary waves in the vicinity of magnetic reconnection events (*Graham et al.*, 2016; *Khotyaintsev et al.*, 2017; *Chang et al.*, 2022).

3.4 Conclusion

In summary, this study expanded upon the work of *Wilder et al.* (2021) in attempting to determine possible correlations between ESWs and observable parameters. Doing so would help to confirm or correct the hypotheses formed, as well as allow for the exploration of previously unobserved relations between solar wind parameters in KHI. In seeking to find these relations, this study additionally observed behaviors correlating between ESWs and local temperature isotropy, observing different behaviors between electrons and ions. These findings suggested that prevalence of ESWs can influence local plasma temperatures.

For global parameters, significant correlations, according to the p-value cutoff of 0.05, were found for every parameter except solar wind temperature and number density. Despite this seemingly overabundance of significant correlations, further analysis showed that some parameters showed a far higher explanation of variance. Namely, the absolute value of the GSE y-coordinate of the event, solar wind pressure, and solar wind bulk velocity all appeared to be heavily associated with the occurrence of ESWs, with the GSE y-coordinate showing the strongest relation by far. These findings seem to partially agree with the hypotheses posed by the previous study, but new questions for further study have now been raised.

Seeing the correlations established in this study, it would be worthwhile to see if the observations could be reproduced by particle-in-cell simulations. Additionally, simulations may be able to see the changes to a KHI by changing the relevant solar wind parameters. If a simulation shows an increased turbulence resulting from increased solar wind pressure and bulk velocity, while the turbulence decreases as the KHI vortices increase in size, it would be extremely compelling supporting evidence of the conclusions formed here.

It is also noteworthy that the geometry of the magnetosphere is nonlinear, and so linear analysis may have its shortcomings in this analysis. It may be prudent to observe results from both non-linear regressions and a multivariate analysis rather than comparing individual parameters one by one. For example, a higher correlation may be found if both GSE x- and y-coordinates are used simultaneously to attempt to explain variation in ESWs, since both relate to the distance along the magnetospheric flanks.

APPENDICES

APPENDIX A

KHI Event Data Plots

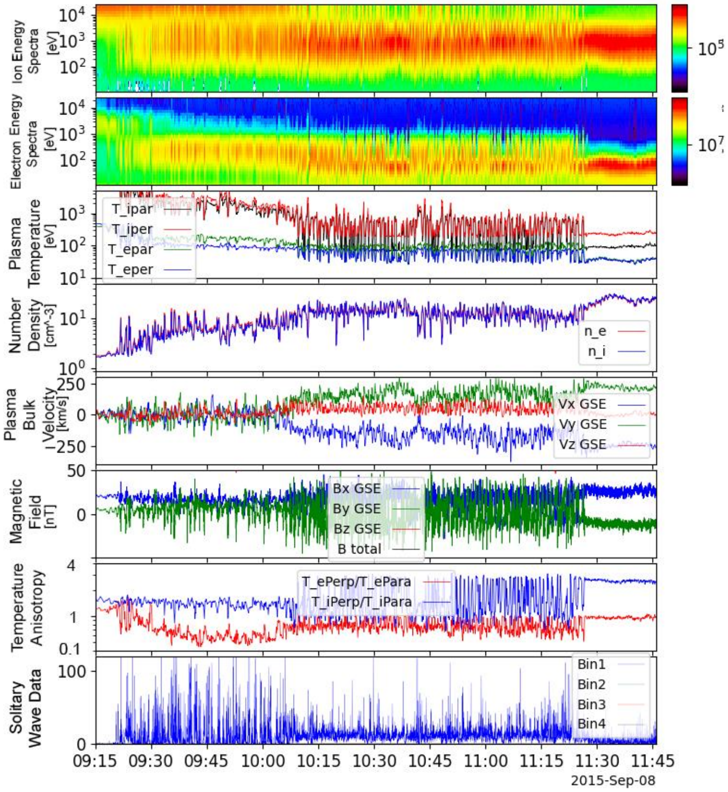

September 8, 2015 Event

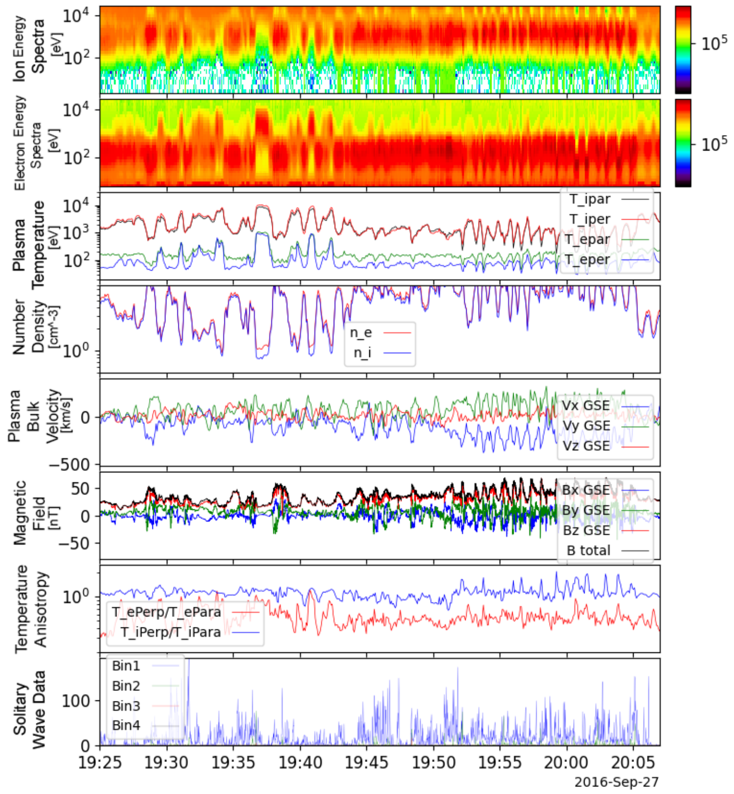

September 27, 2016 Event

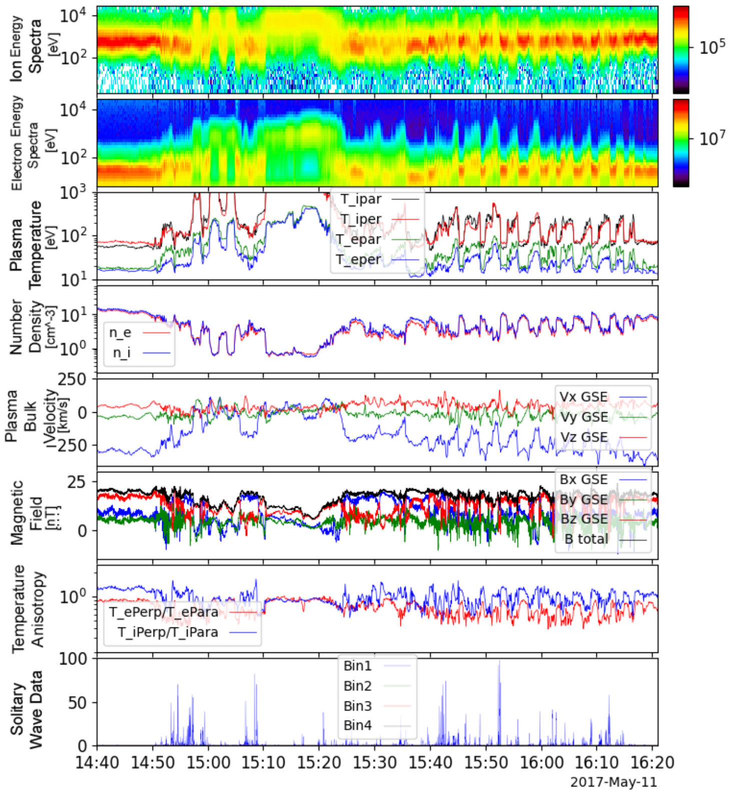

May 11, 2017 Event

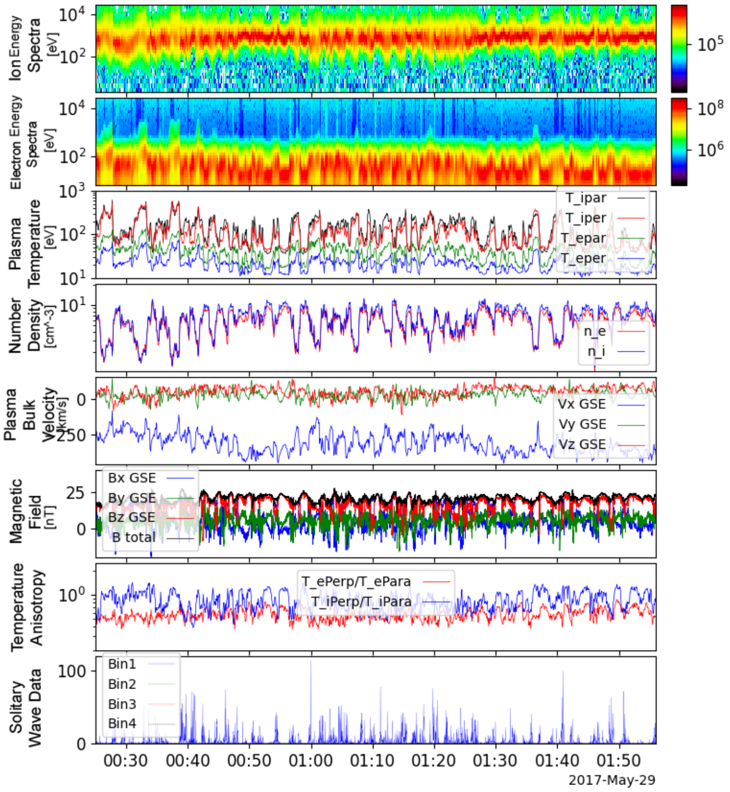

May 29, 2017 Event

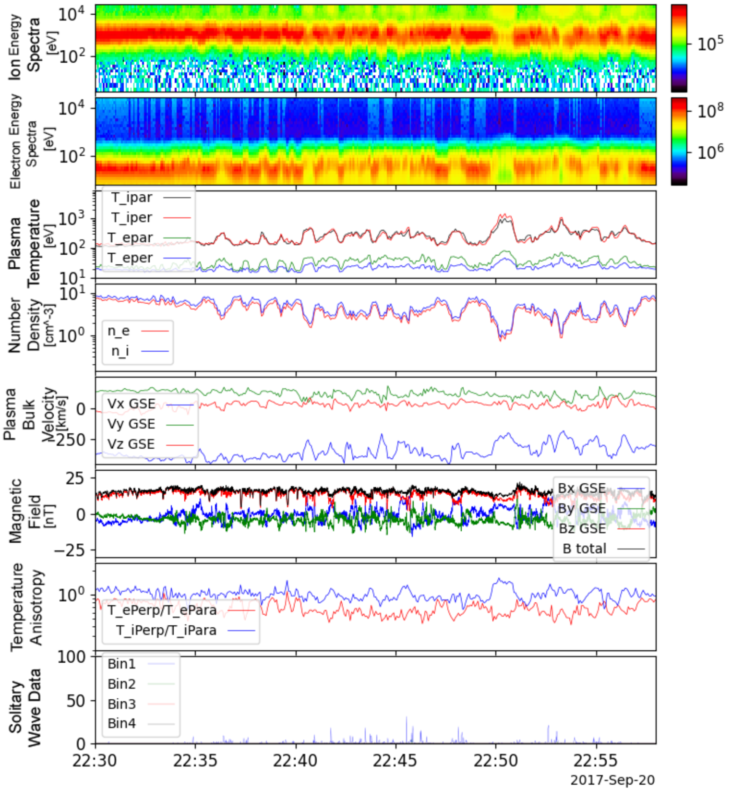

September 20, 2017 Event

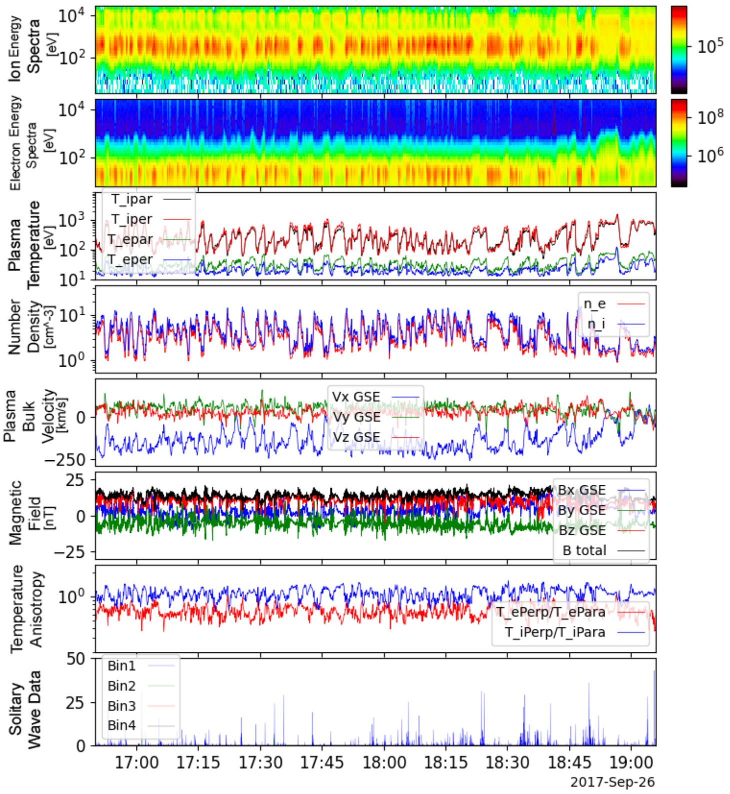

September 26, 2017 Event

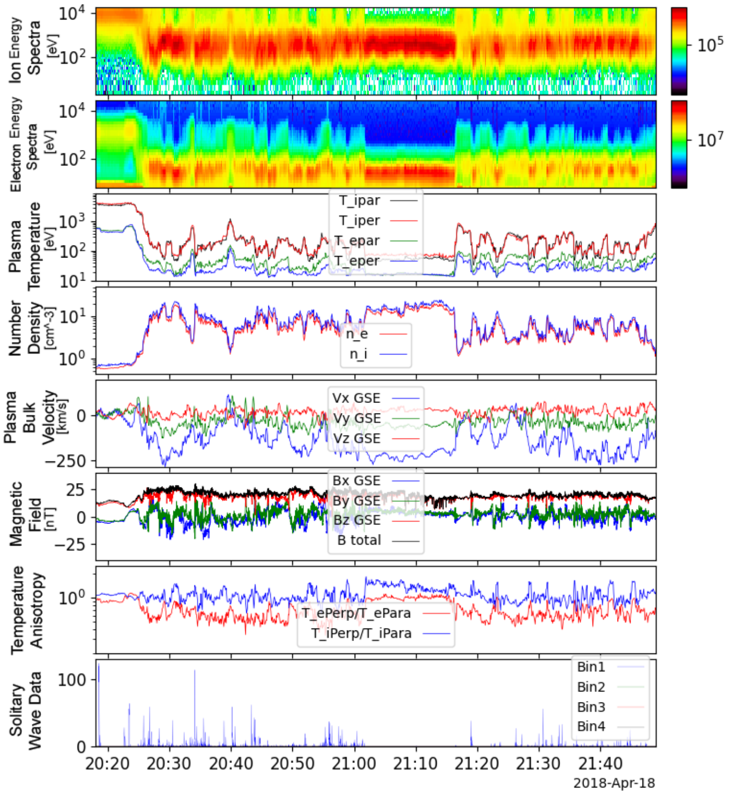

April 18, 2018 Event

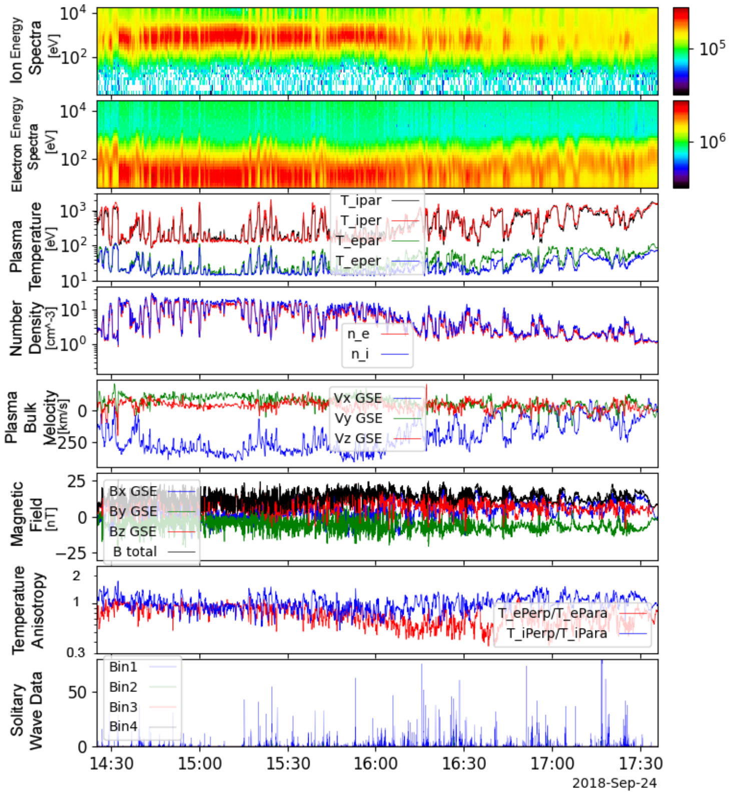

September 24, 2018 Event

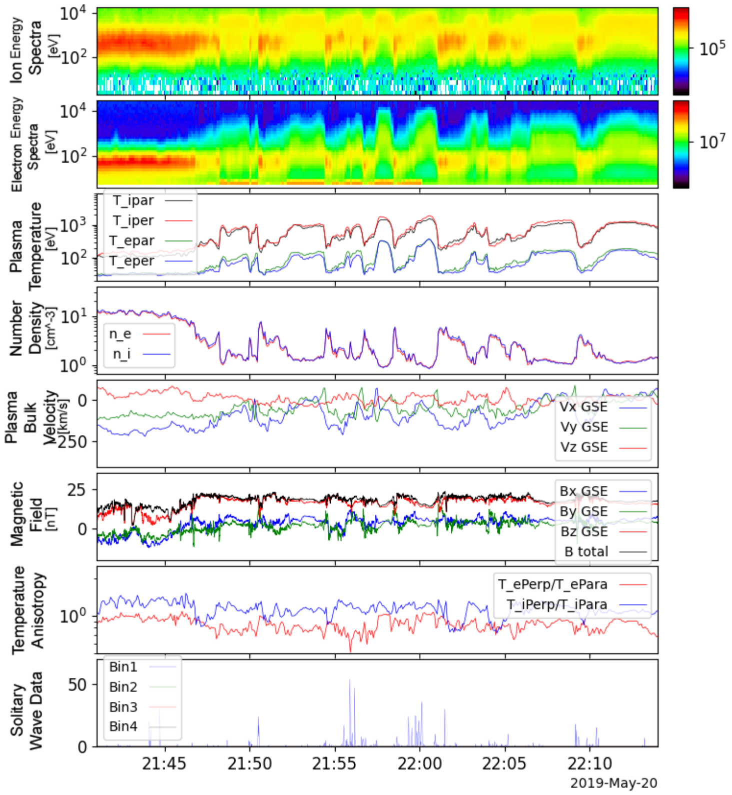

May 20, 2019 Event

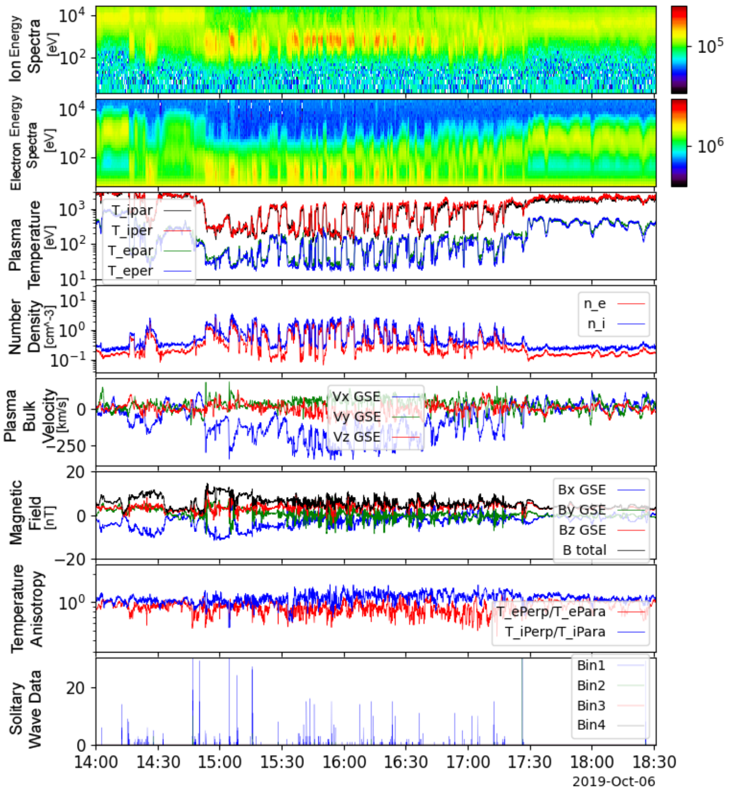

October 6, 2019 Event

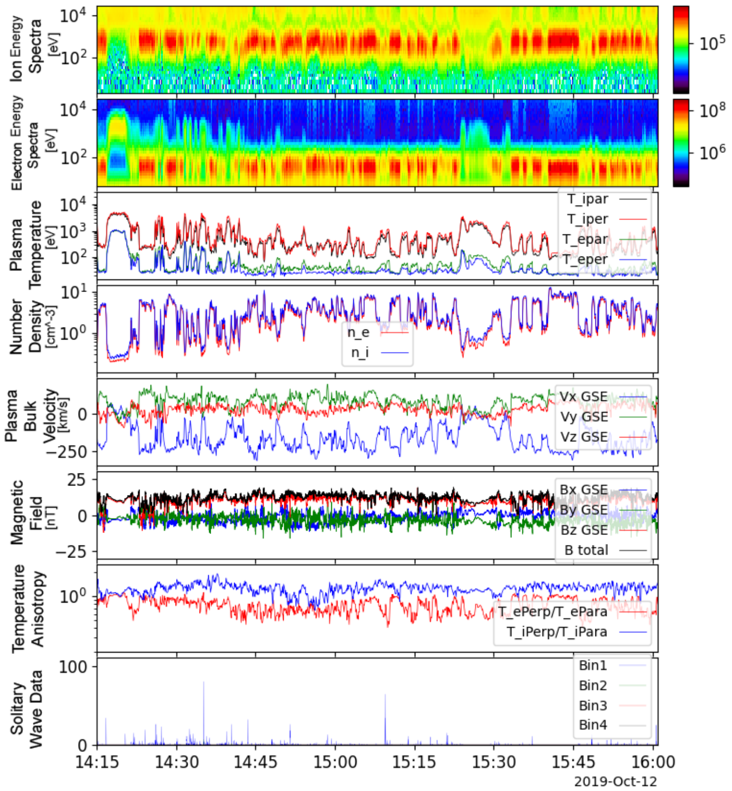

October 12, 2019 Event

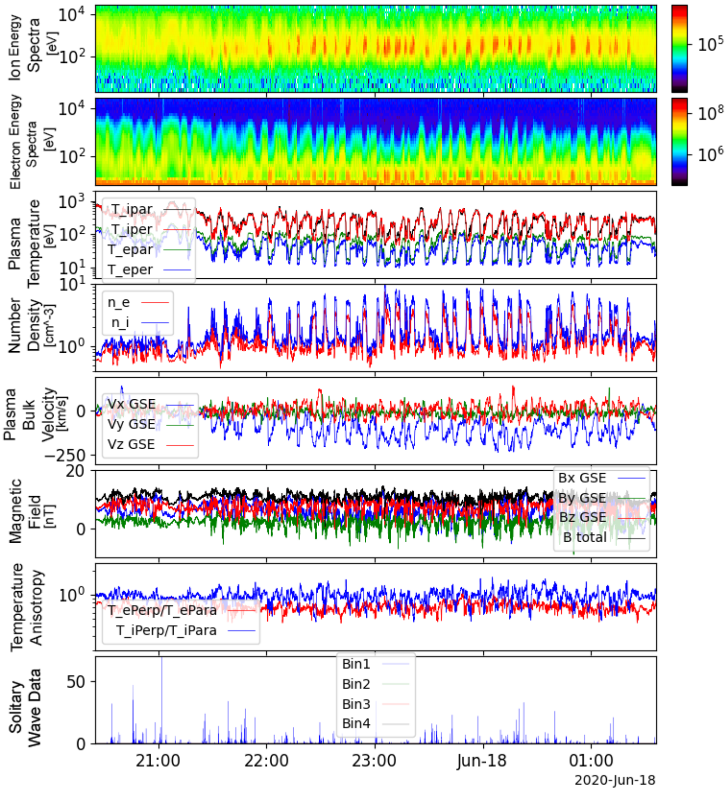

June 17-18, 2020 Event

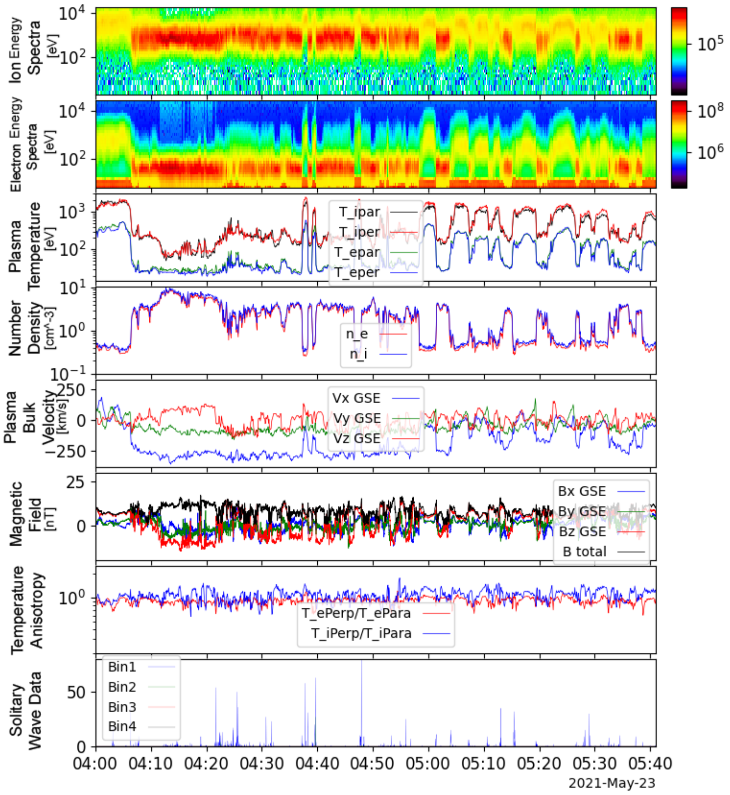

May 23, 2021 Event

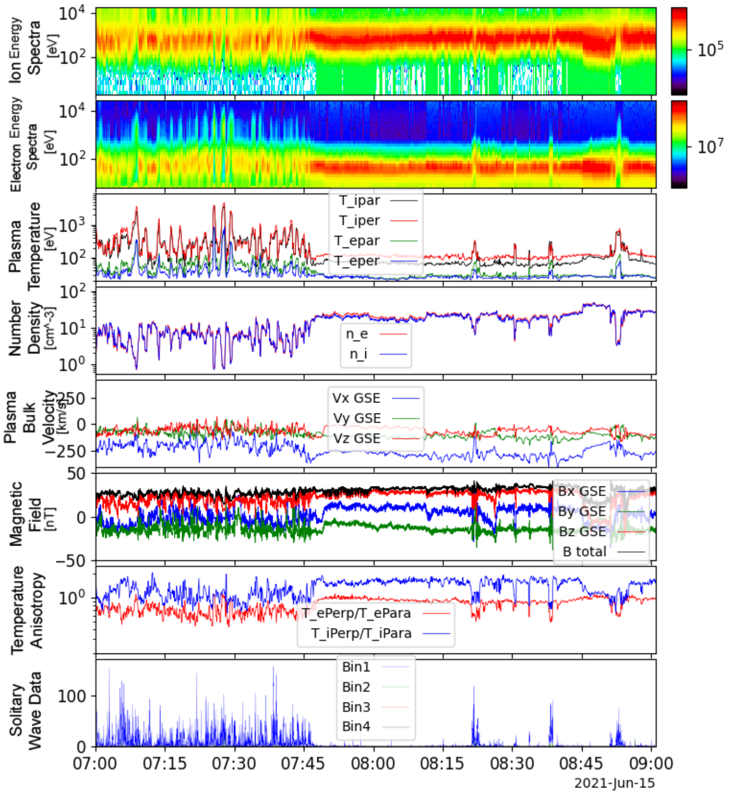

June 15, 2021 Event

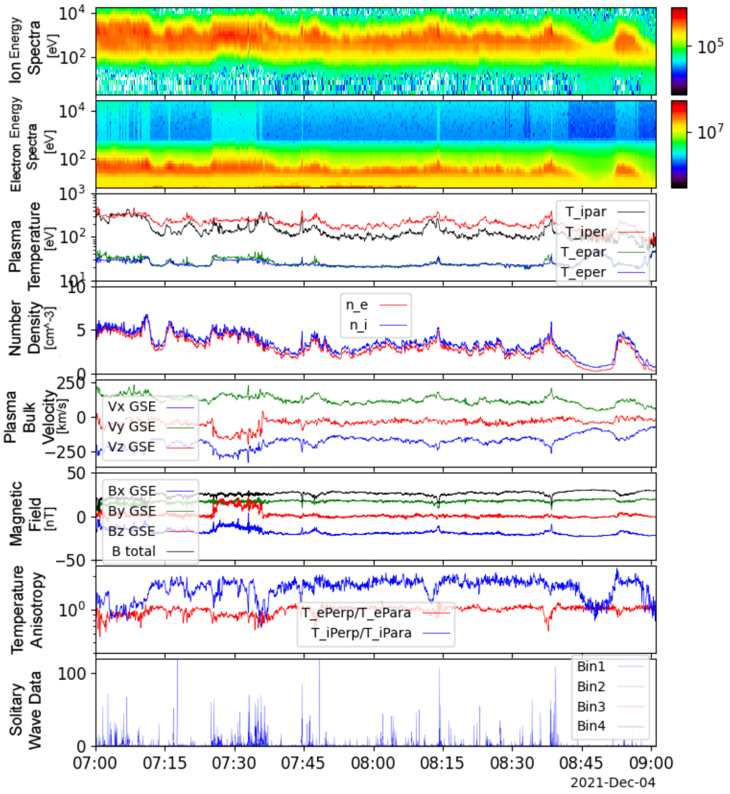

December 4, 2021 Event

APPENDIX B

Solitary Wave Counts as a Function of Temperature Anisotropy

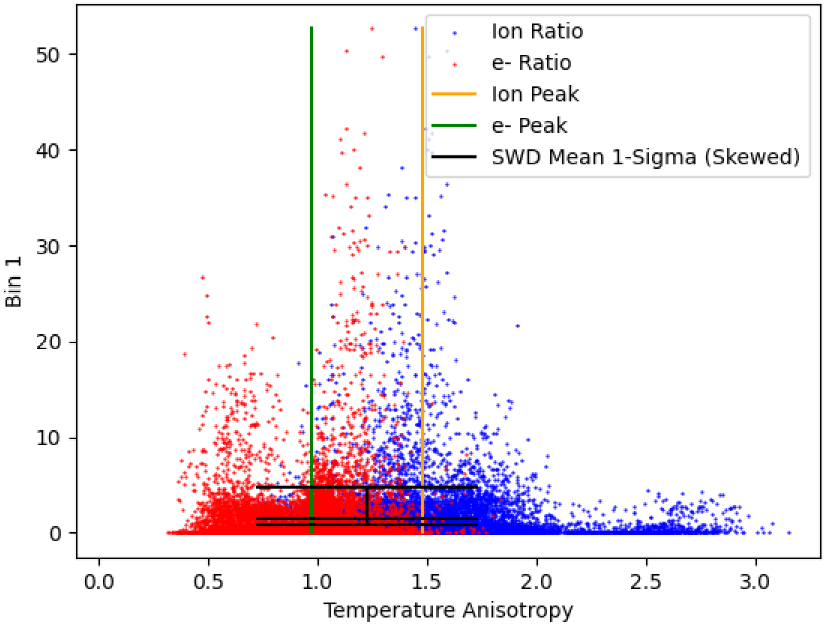

Solitary Waves (<1 mV/m) as a function of temperature anisotropy for ions and electrons, with associated peak function. September 8, 2015 Event

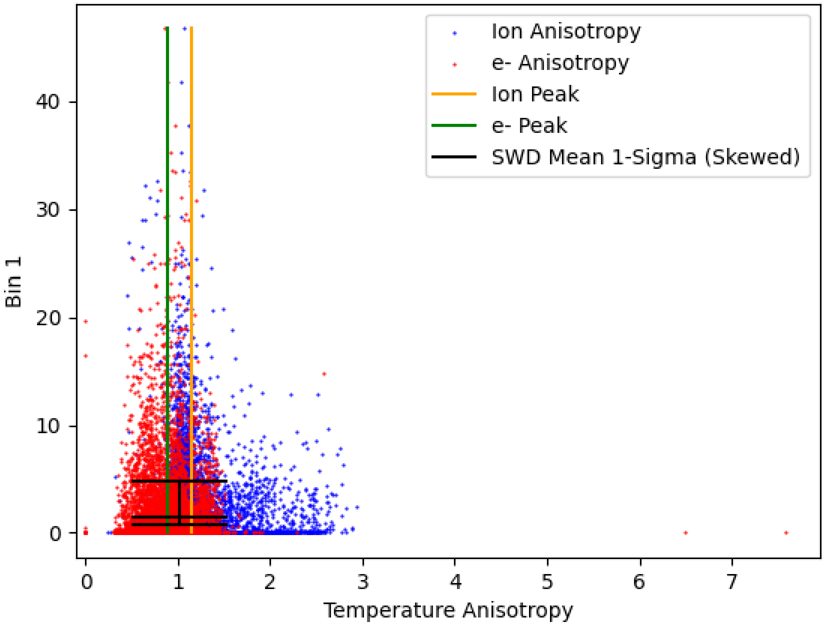

Solitary Waves (<1 mV/m) as a function of temperature anisotropy for ions and electrons, with associated peak function. September 27, 2016 Event

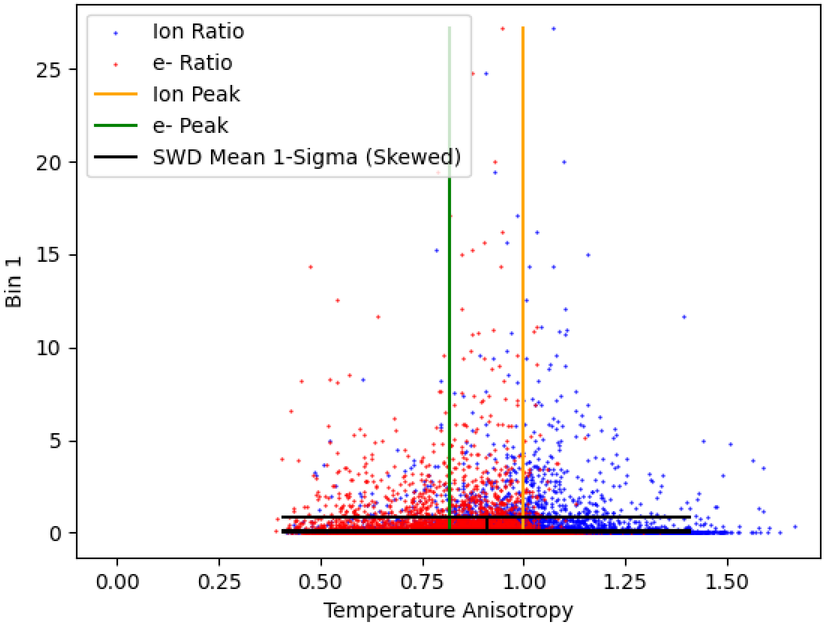

Solitary Waves (<1 mV/m) as a function of temperature anisotropy for ions and electrons, with associated peak function. May 11, 2017 Event

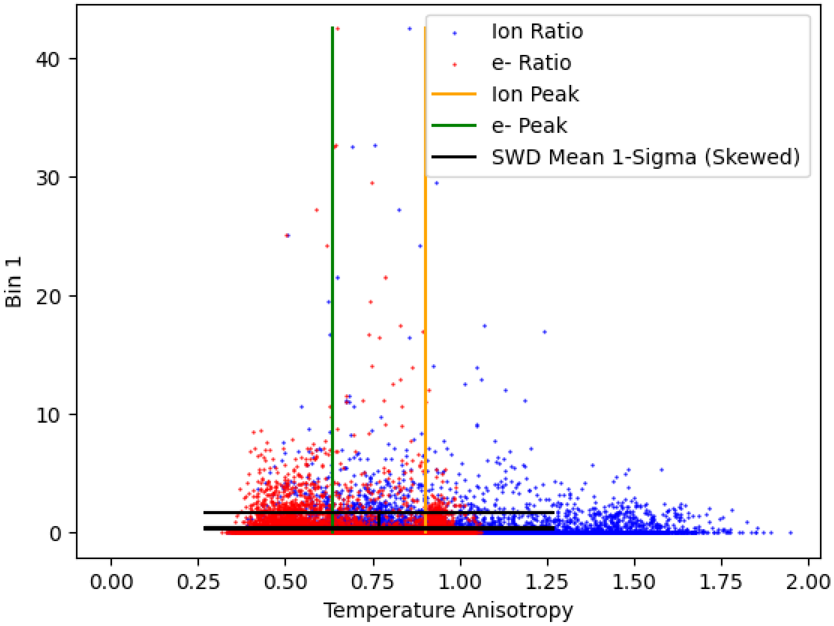

Solitary Waves (<1 mV/m) as a function of temperature anisotropy for ions and electrons, with associated peak function. May 29, 2017 Event

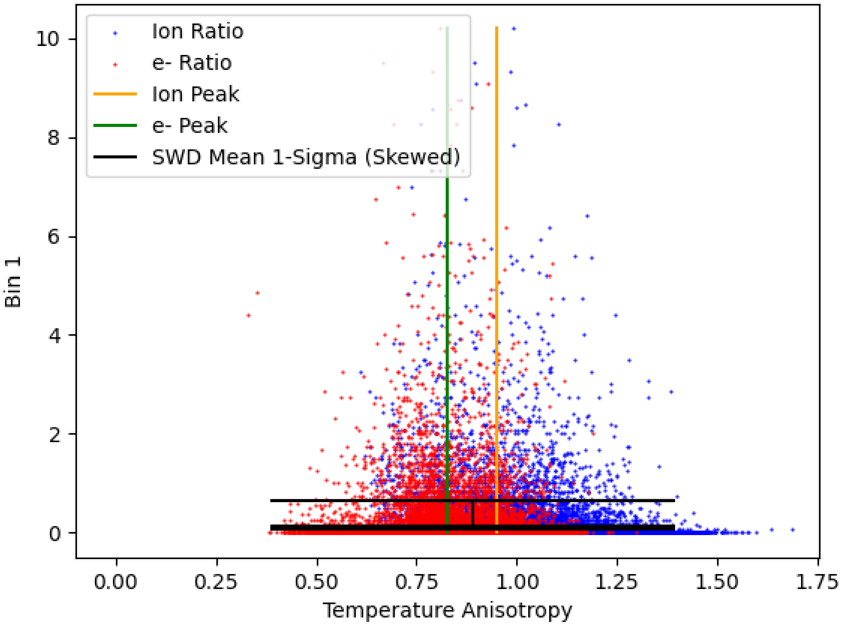

Solitary Waves (<1 mV/m) as a function of temperature anisotropy for ions and electrons, with associated peak function. September 20, 2017 Event

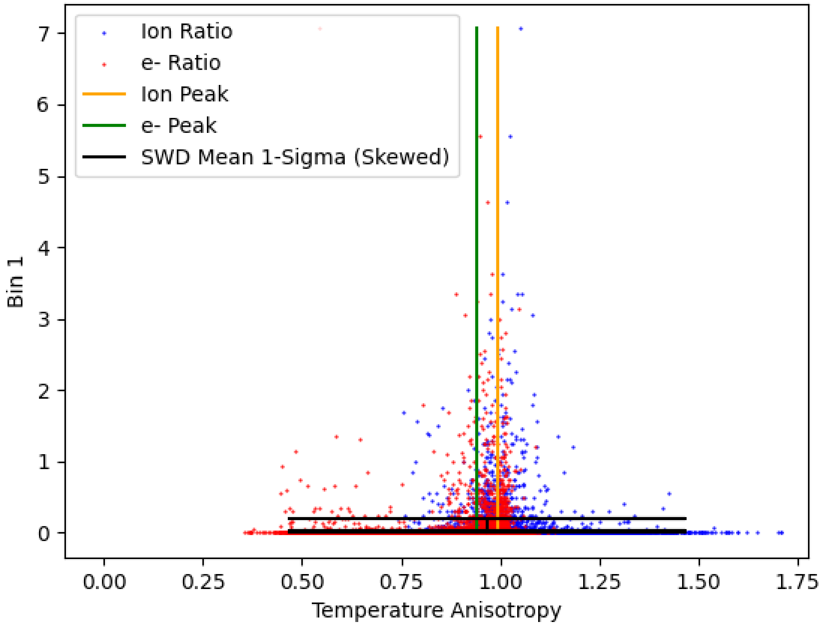

Solitary Waves (<1 mV/m) as a function of temperature anisotropy for ions and electrons, with associated peak function. September 26, 2017 Event

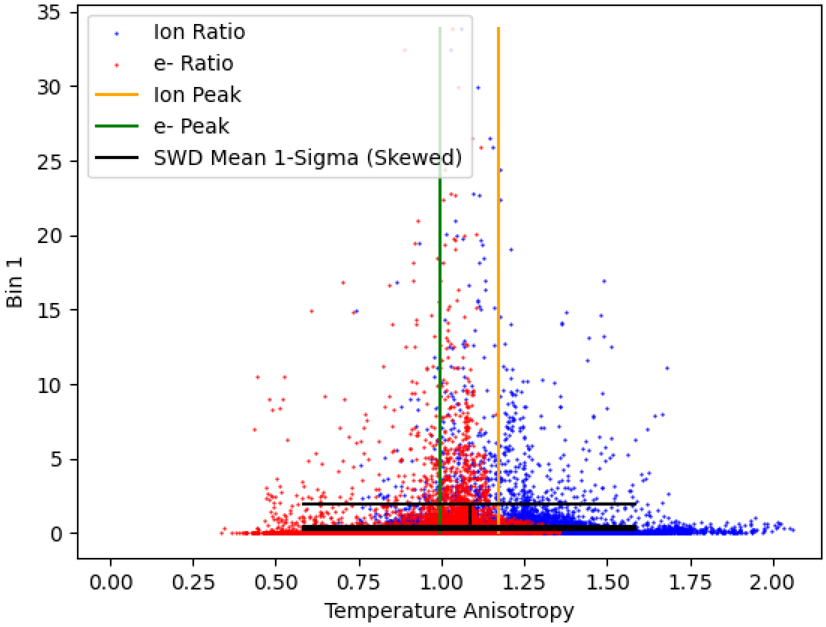

Solitary Waves (<1 mV/m) as a function of temperature anisotropy for ions and electrons, with associated peak function. April 18, 2018 Event

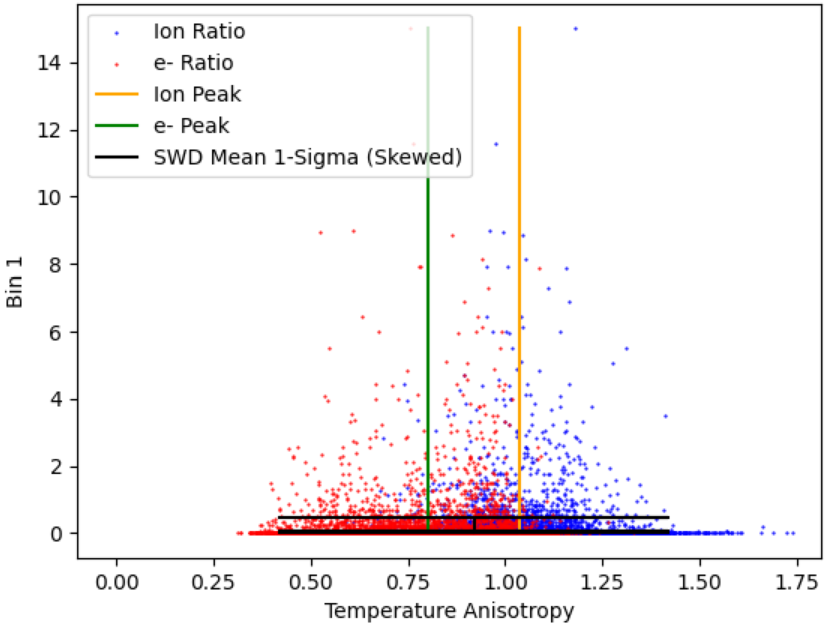

Solitary Waves (<1 mV/m) as a function of temperature anisotropy for ions and electrons, with associated peak function. September 24, 2018 Event

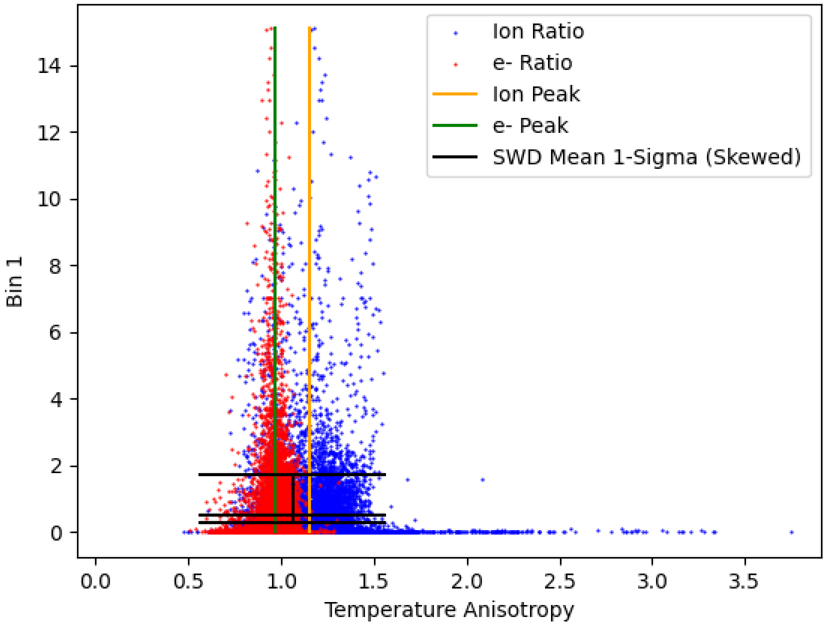

Solitary Waves (<1 mV/m) as a function of temperature anisotropy for ions and electrons, with associated peak function. May 20, 2019 Event

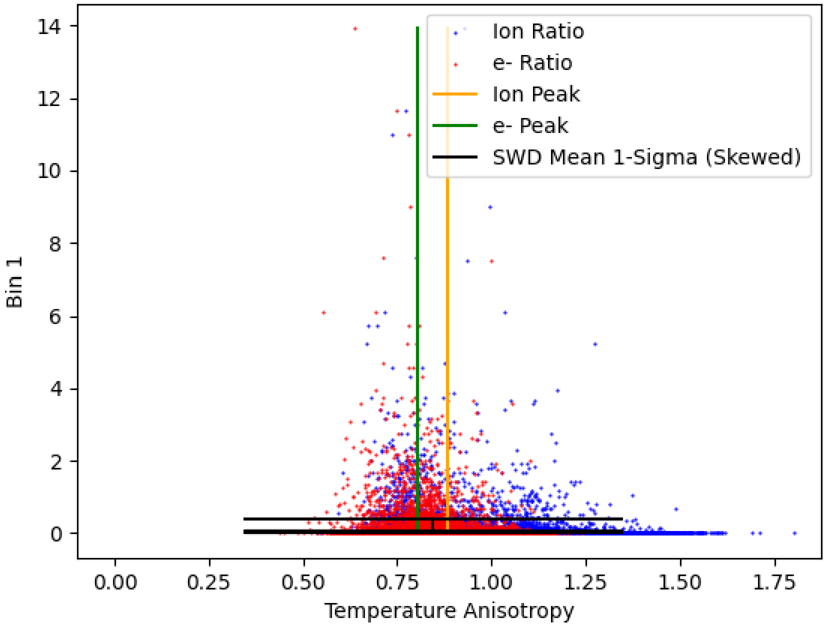

Solitary Waves (<1 mV/m) as a function of temperature anisotropy for ions and electrons, with associated peak function. October 6, 2019 Event

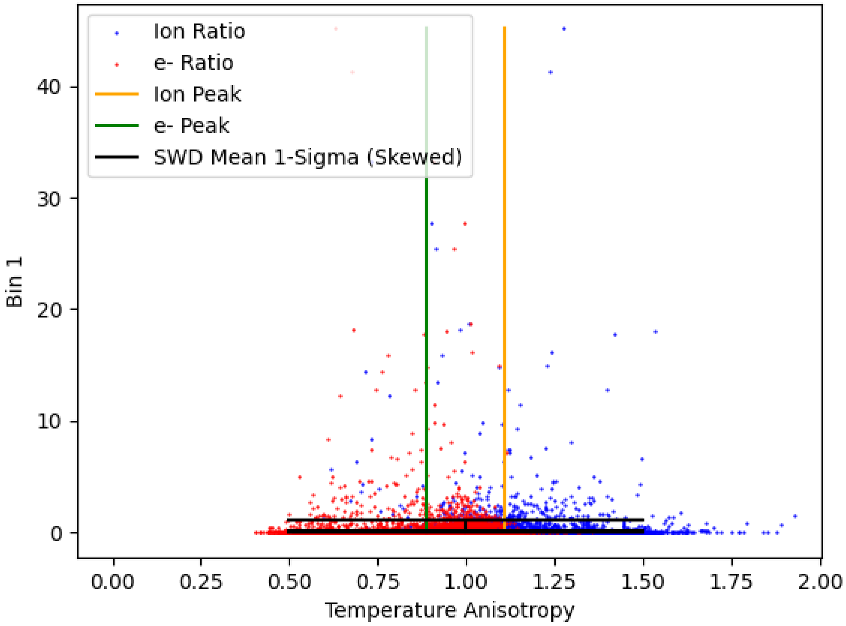

Solitary Waves (<1 mV/m) as a function of temperature anisotropy for ions and electrons, with associated peak function. October 12, 2019 Event

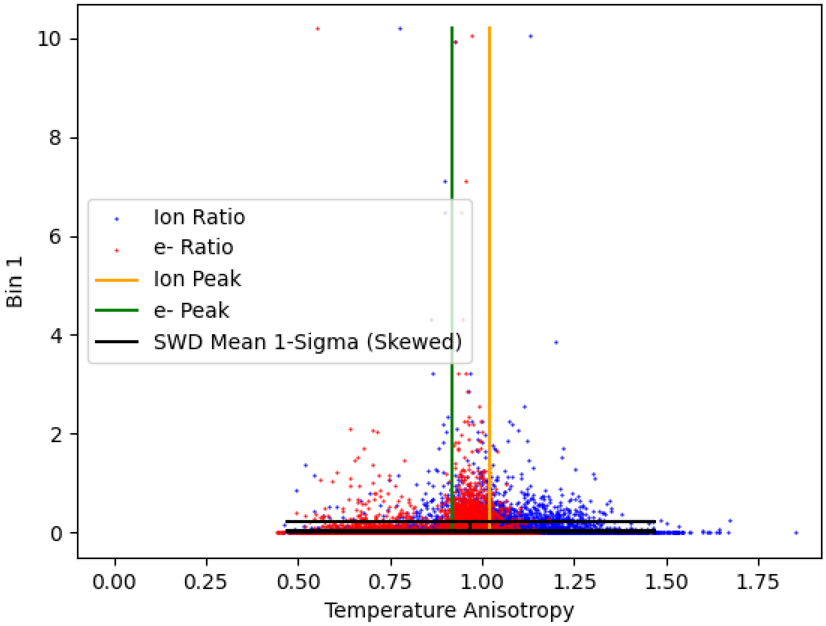

Solitary Waves (<1 mV/m) as a function of temperature anisotropy for ions and electrons, with associated peak function. June 17-18, 2020 Event

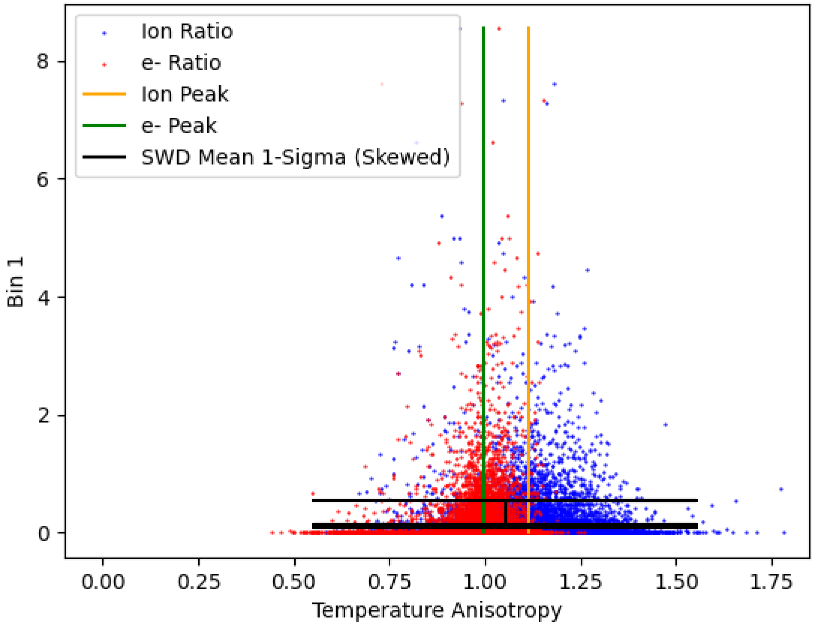

Solitary Waves (<1 mV/m) as a function of temperature anisotropy for ions and electrons, with associated peak function. May 23, 2021 Event

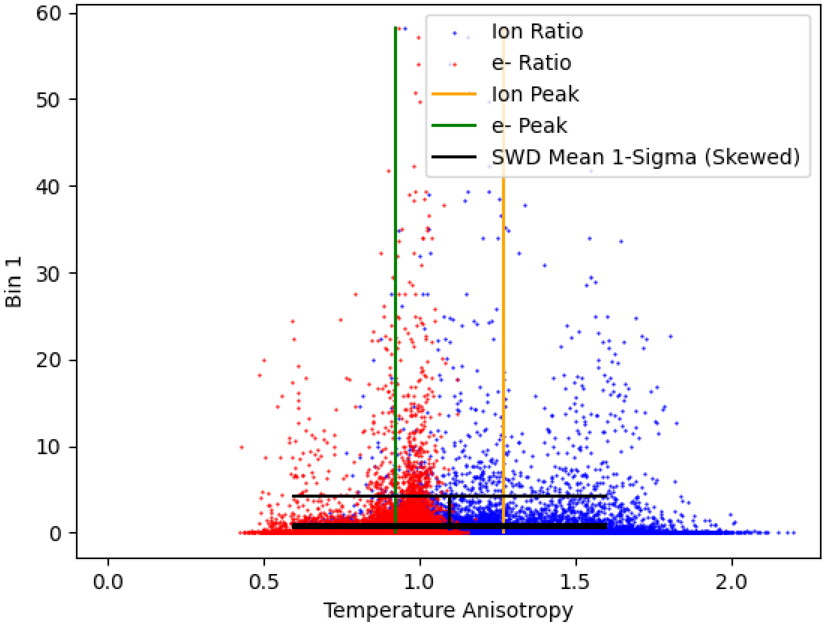

Solitary Waves (<1 mV/m) as a function of temperature anisotropy for ions and electrons, with associated peak function. June 15, 2021 Event

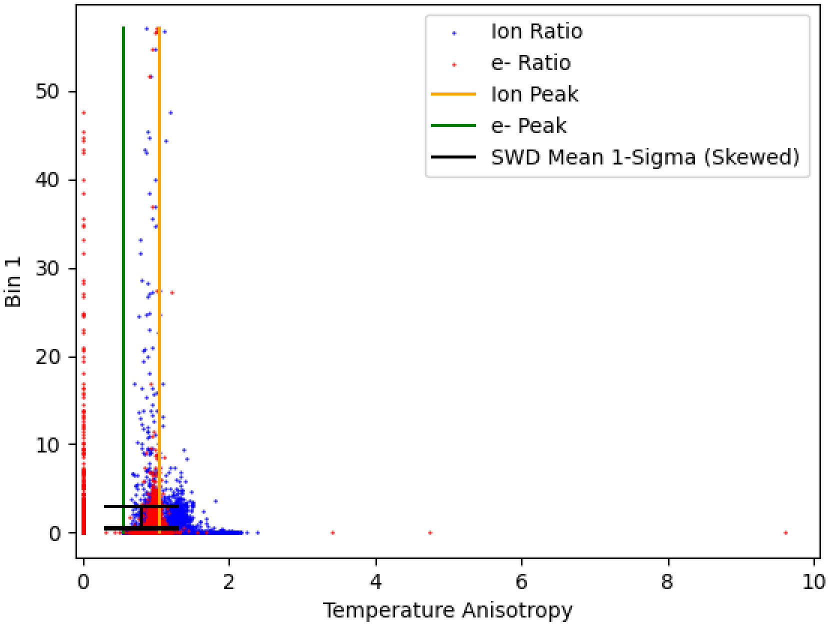

Solitary Waves (<1 mV/m) as a function of temperature anisotropy for ions and electrons, with associated peak function. December 4, 2021 Event. Possible "null" value counting

APPENDIX C

Average Solitary Wave Counts as a Function of Various Parameters

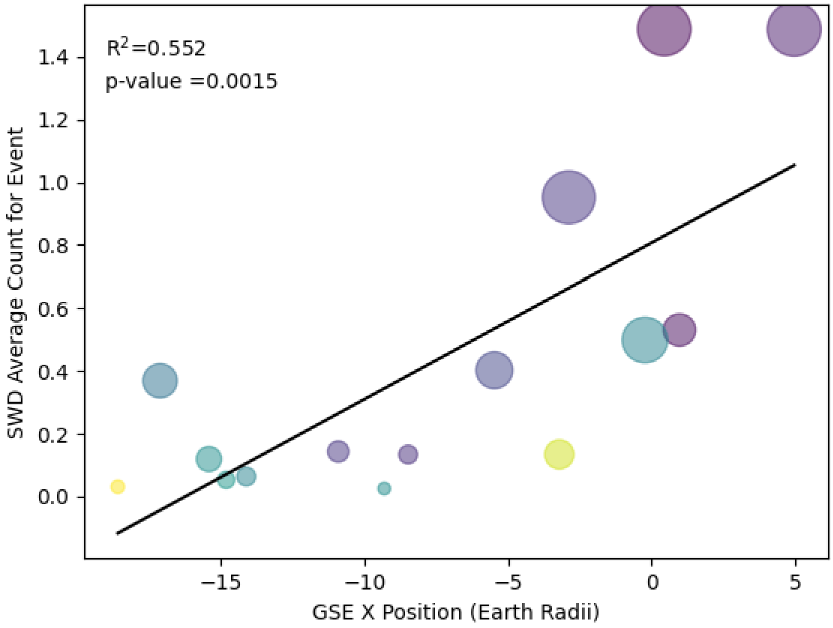

Average Solitary Wave Count as a function of GSE x-coordinate. Larger dot size indicates a higher standard deviation, while a lighter dot color indicates a higher skew.

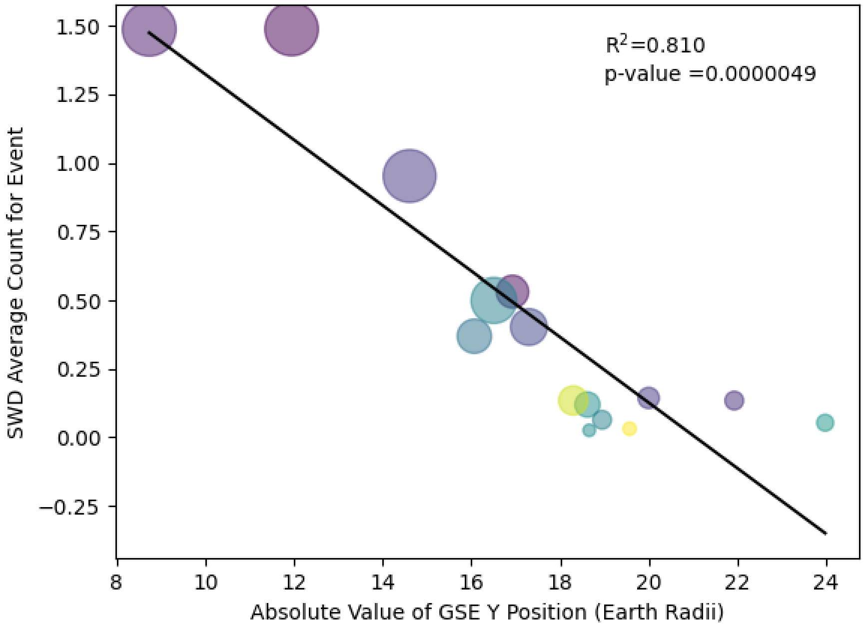

Average Solitary Wave Count as a function of the absolute value of the GSE y-coordinate. Larger dot size indicates a higher standard deviation, while a lighter dot color indicates a higher skew.

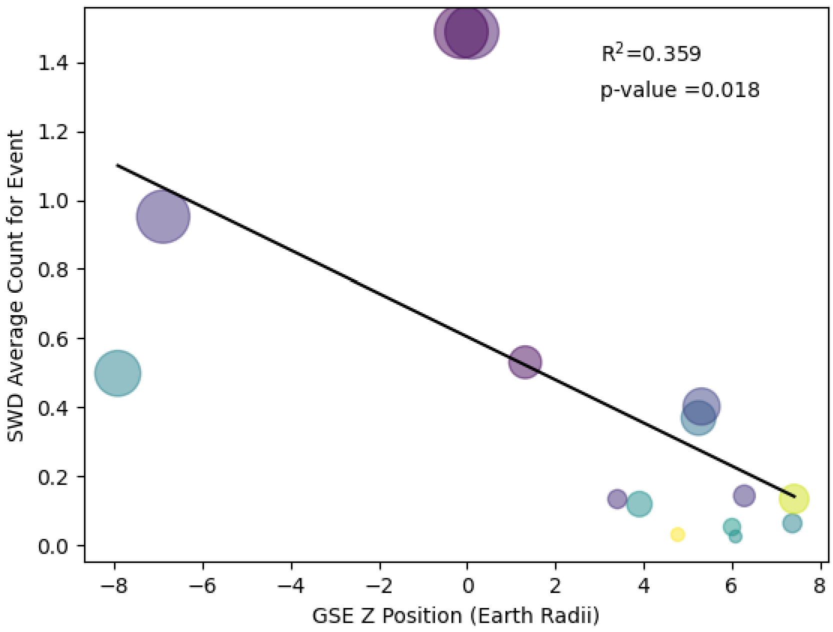

Average Solitary Wave Count as a function of GSE z-coordinate. Larger dot size indicates a higher standard deviation, while a lighter dot color indicates a higher skew.

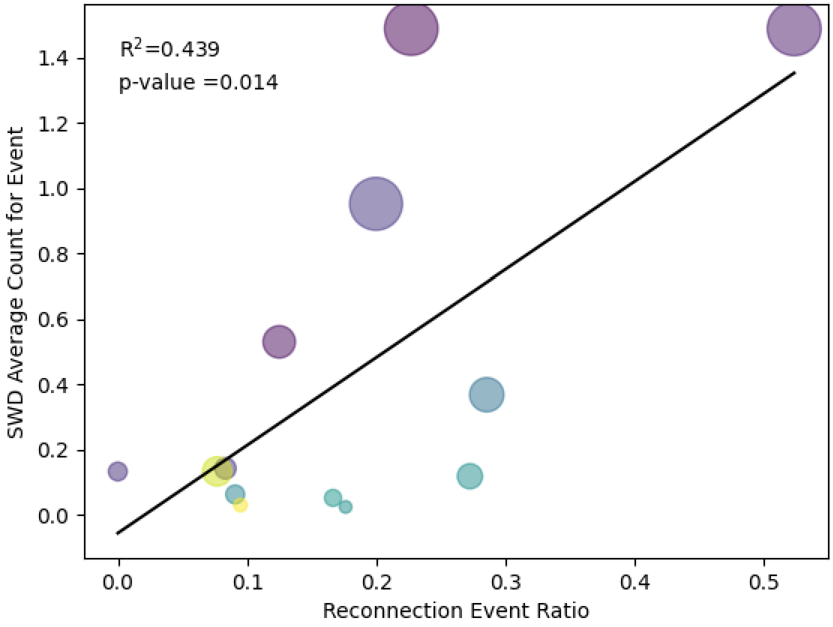

Average Solitary Wave Count as a function of the reconnection ratio. Larger dot size indicates a higher standard deviation, while a lighter dot color indicates a higher skew.

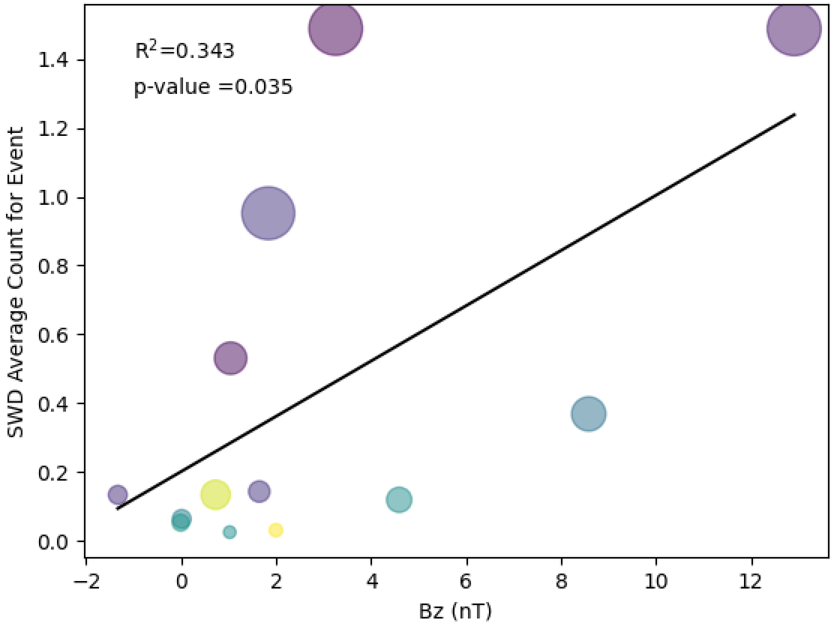

Average Solitary Wave Count as a function of the solar wind magnetic field along the GSM z-axis. Larger dot size indicates a higher standard deviation, while a lighter dot color indicates a higher skew.

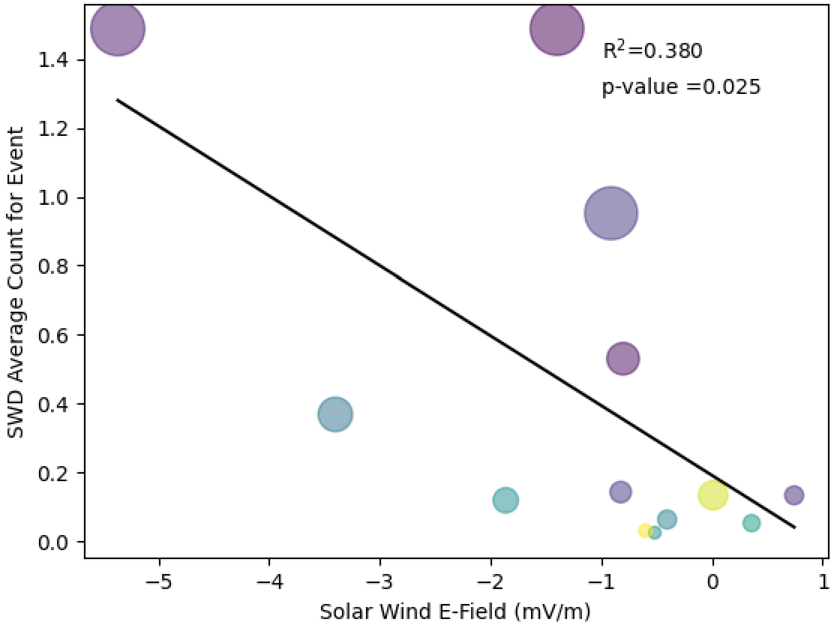

Average Solitary Wave Count as a function of solar wind electric field strength. Larger dot size indicates a higher standard deviation, while a lighter dot color indicates a higher skew.

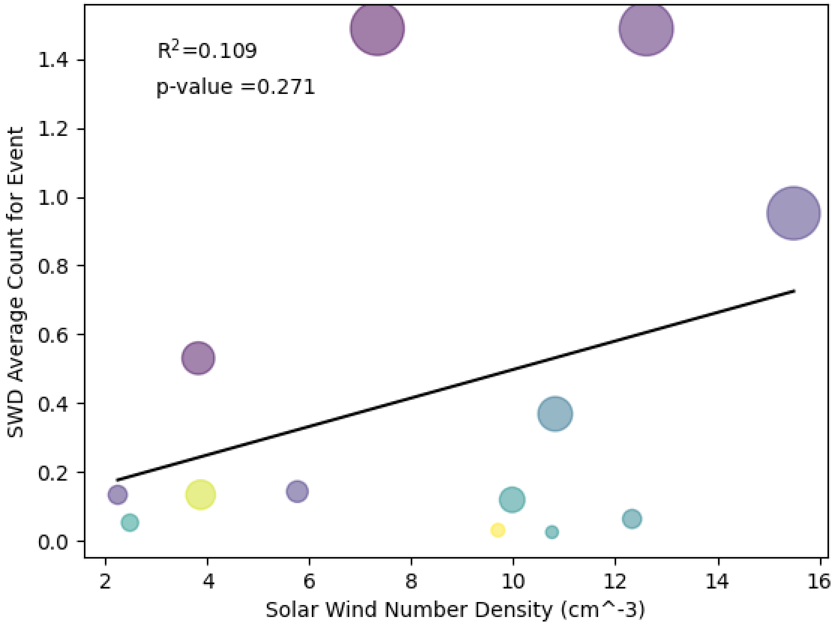

Average Solitary Wave Count as a function of the solar wind number density. Larger dot size indicates a higher standard deviation, while a lighter dot color indicates a higher skew.

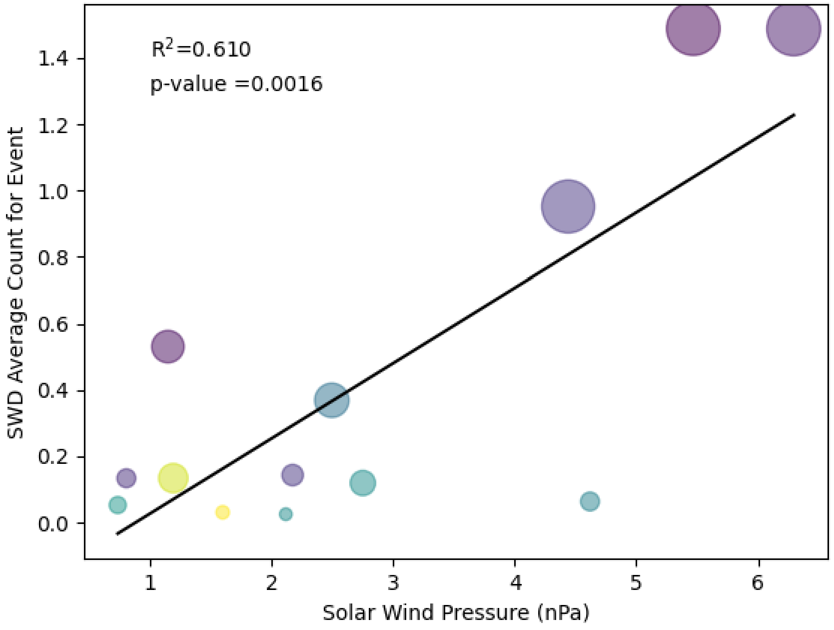

Average Solitary Wave Count as a function of the solar wind pressure. Larger dot size indicates a higher standard deviation, while a lighter dot color indicates a higher skew.

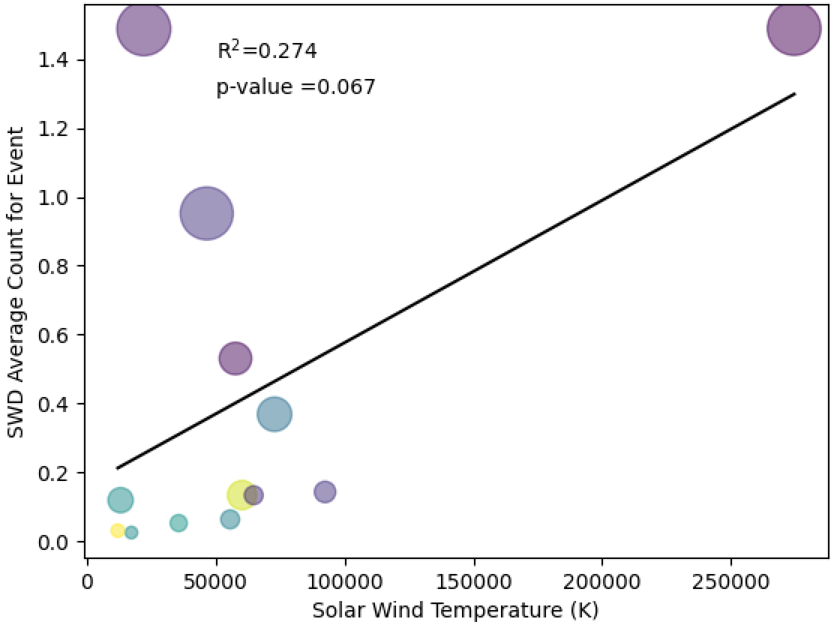

Average Solitary Wave Count as a function of the solar wind temperature. Larger dot size indicates a higher standard deviation, while a lighter dot color indicates a higher skew.

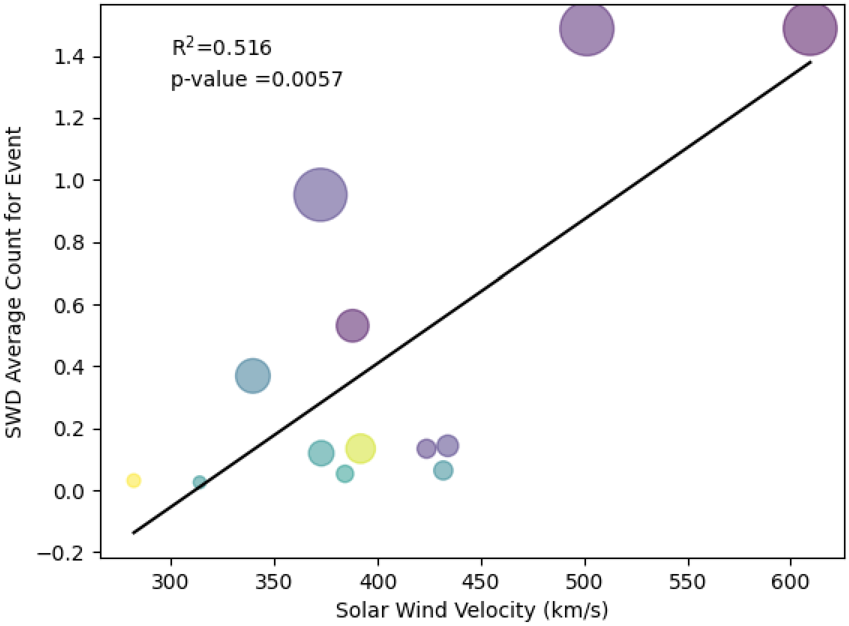

Average Solitary Wave Count as a function of solar wind velocity. Larger dot size indicates a higher standard deviation, while a lighter dot color indicates a higher skew.

BIBLIOGRAPHY

Axford, W. Ian, and Colin O. Hines. "A unifying theory of high-latitude geophysical phenomena and geomagnetic storms." *Canadian Journal of Physics* 39.10 (1961): 1433-1464.

Buneman, O., “Excitation of field aligned sound waves by electron streams.” *Physical Review Letters,* 10.7 (1963): 285.

Burch, J.L., Torbert, R.B. “Preface”. *Space Sci Rev* 199 (2015): 1–3. DOI: 10.1007/s11214-015-0153-z

Chang, C., et al. "Electrostatic Solitary Waves and Electron-beam Instabilities in the Separatrix Region of Magnetic Reconnection." *The Astrophysical Journal* 933.1 (2022): 67.

Chapman, S., and V. C. A. Ferraro. "Terrestrial magnetism and atmospheric electricity." *J. Geophys. Res* 36.77-97 (1931): 171-186.

Cowley, S. W. H. "Magnetosphere-ionosphere interactions: A tutorial review." *Magnetospheric Current Systems, Geophys. Monogr. Ser 118* (2000), 91-106.

Dorelli, John C., Amitava Bhattacharjee, and Joachim Raeder. "Separator reconnection at Earth's dayside magnetopause under generic northward interplanetary magnetic field conditions." *Journal of Geophysical Research: Space Physics* 112.A2 (2007).

Dungey, J. W., “Physics of the Ionosphere: Electrodynamics of the outer atmosphere,” *The Physical Society of London* (1955). 229

Dungey, J. W., "Interplanetary magnetic field and the auroral zones." *Physical Review Letters* 6.2 (1961): 47.

Ergun, R. E., et al. "The axial double probe and fields signal processing for the MMS mission." *Space Science Reviews* 199 (2016): 167-188.

Faganello, Matteo, and Francesco Califano. "Magnetized Kelvin–Helmholtz instability: theory and simulations in the Earth's magnetosphere context." *Journal of Plasma Physics* 83.6 (2017): 535830601.

Graham, D. B., Khotyaintsev, Y. V., Vaivads, A., & Andre, M. "Electrostatic solitary waves and electrostatic waves at the magnetopause." *Journal of Geophysical Research: Space Physics*, 121.4 (2016), 3069-3092.

Gurnett, Donald A., and Amitava Bhattacharjee. *Introduction to Plasma Physics: With Space and Laboratory Applications.* Cambridge University Press, 2005.

Hansel, Paul James, et al. "Mapping MMS observations of solitary waves in Earth's magnetic field." *Journal of Geophysical Research: Space Physics* 126.12 (2021): e2021JA029389.

Hapgood, M. A. "Space physics coordinate transformations: A user guide." *Planetary and Space Science* 40.5 (1992): 711-717.

Helmholtz. "XLIII. On discontinuous movements of fluids." *The London, Edinburgh, and Dublin Philosophical Magazine and Journal of Science* 36.244 (1868): 337-346.

Hundhausen, A. J., M. G. Kivelson, and C. T. Russell. “The Solar Wind” *Introduction to Space Physics* (1995): 90-128.

Hwang, K. J., et al. "Bifurcated Current Sheet Observed on the Boundary of Kelvin-Helmholtz Vortices." *Frontiers in Astronomy and Space Sciences* 8 (2021): 782924.

Kaase, Aaron. “Earth’s Magnetosphere.” Edited by Holly Zell, *NASA*, 2 Mar. 2015, www.nasa.gov/mission_pages/sunearth/multimedia/magnetosphere.html.

Kavosi, Shiva, and Joachim Raeder. "Ubiquity of Kelvin–Helmholtz waves at Earth’s magnetopause." *Nature Communications* 6.1 (2015): 7019.

Kelvin, W. T. "Hydrokinetic solutions and observation." *Philosophical Magazine* 42 (1871): 362-377.

King, J. H., and N. E. Papitashvili. “One min and 5-min solar wind data sets at the Earth's bow shock nose” *NASA Goddard Space Flight Center* (Updated 2023)

King, J. H., and N. E. Papitashvili. "Solar wind spatial scales in and comparisons of hourly Wind and ACE plasma and magnetic field data." Journal of Geophysical Research: Space Physics 110.A2 (2005).

Khotyaintsev, Yuri, et al. "Multi-spacecraft Observation of Electrostatic Solitary Waves in the Reconnection Separatrix Region." *EGU General Assembly Conference Abstracts.* 2017

Kivelson, Margaret Galland, and Christopher T. Russell, eds. *Introduction to Space Physics*. Cambridge University Press, 1995.

Laundal, Karl Magnus, and Arthur D. Richmond. "Magnetic Coordinate Systems." *Space Science Reviews* 206.1-4 (2017): 27-59.

Lindqvist, P-A., et al. "The spin-plane double probe electric field instrument for MMS." *Space Science Reviews* 199 (2016): 137-165.

Mozer, F. S., et al. "Time domain structures: What and where they are, what they do, and how they are made." *Geophysical Research Letter*s 42.10 (2015): 3627-3638.

Muschietti, L., et al. "Phase-space electron holes along magnetic field lines." *Geophysical Research Letters* 26.8 (1999): 1093-1096.

Papitashvili, Natalia E. and King, Joseph H. (2020), "OMNI 1-min Data", *NASA Space Physics Data Facility,* DOI: 10.48322/45bb-8792

Parker, E. N. "Dynamics of the interplanetary gas and magnetic fields." *Astrophysical Journal*, 128 (1958): 664.

Parker, E. N. "Dynamical theory of the solar wind." *Space Science Reviews* 4.5-6 (1965): 666-708.

Paschmann, G., et al. "The magnetopause for large magnetic shear: AMPTE/IRM observations." *Journal of Geophysical Research: Space Physics* 91.A10 (1986): 11099-11115.

Pedersen, A., et al. "Electron density estimations derived from spacecraft potential measurements on Cluster in tenuous plasma regions." *Journal of Geophysical Research: Space Physics* 113.A7 (2008).

Pollock, C., et al. "Fast plasma investigation for magnetospheric multiscale." *Space Science Reviews* 199 (2016): 331-406.

Russell, C. T., et al. "The magnetospheric multiscale magnetometers." *Space Science Reviews* 199 (2016): 189-256.

Seki, K., et al. "A review of general physical and chemical processes related to plasma sources and losses for solar system magnetospheres." 192 (2015): 27-89.

Sibeck, D. G., et al. "ARTEMIS science objectives." *The ARTEMIS mission* (2014): 27-59.

Singh, R. “Coupling of the Solar Driven Prolonged and Transient Processes to the Equitorial and Low Latitude Ionosphere.” *Indian Institute of Geomagnetism* (2019).

Sonnerup, B. U., and M. Scheible. "Minimum and maximum variance analysis." *Analysis methods for multi-spacecraft data* (1998): 185-220.

Störmer, Carl. "Sur les trajectoires des corpuscules électrisés dans l'espace sous l'action du magnétisme terrestre, avec application aux aurores boréales. (On the trajectories of electrified corpuscles in space under the action of terrestrial magnetism, with application to the aurora borealis)" *Le Radium* 9.11 (1912): 395-399.

Temerin, M., et al. "Observations of double layers and solitary waves in the auroral plasma." *Physical Review Letters* 48.17 (1982): 1175.

Vasko, I. Y., et al. "Electron-acoustic solitons and double layers in the inner magnetosphere." *Geophysical Research Letters* 44.10 (2017): 4575-4583.

Wilder, F. D., et al. "The Occurrence and Prevalence of Time Domain Structures in the Kelvin-Helmholtz Instability at Different Positions Along the Earth’s Magnetospheric Flanks." *Frontiers in Astronomy and Space Sciences* 8 (2021): 756563

Wilder, F. D., et al. “The occurrence and prevalence of magnetic reconnection in the Kelvin-Helmholtz instability under various solar wind conditions” *Submitted to Journal of Geophysical Research: Space Physics* (2023)